Chapter 3

High–Resolution 3D Simulations of Relativistic Jets

3.1. Extragalactic jets

The first physical application in which we are interested in is the simulation of the dynamical evolution of extragalactic jets and their emission properties. An astrophysical jet is a collimate flux of plasma that some galaxies, quasars, micro-quasars, X-ray binaries, etc., may produce as a consequence of the accretion of matter onto massive objects. In order to motivate our work, we are going to establish the observational framework in which the jet phenomenon is included (Sect. 3.1.1). Then we will outline the standard model which tries to explain the current observations (Sect. 3.1.2). In the next Section (Sect. 3.1.3) an historical overview of the numerical simulations in this field will be given. Section 3.2 includes the results obtained by Aloy *et al.* (1999b), in which we explore the 3D relativistic regime by means of helically perturbed axisymmetric models. Additionally, we will make a comparative study of a set of perturbed models with the one pesented in Aloy *et al.* (1999b). Finally, the emission properties of 3D relativistic jets are evaluated in section 3.3.

3.1.1. Phenomenology

The first detected jet (Curtis 1918) was the one in the giant elliptic galaxy M87. Although this jet was originally seen at optical wavelengths, typical jets are observed at radio frequencies. This explains why the progress in the discovery of new sources is strongly linked to the technical improvements in the radio observations. The first observed radio jets where those associated to powerful radio sources. More precisely, Jennison & Das Gupta (1953) reported that the radio emission from Cygnus A originated from two lobes straddling the associated optical galaxy rather than the galaxy itself. With the advent of the Cambridge 5 km telescope (in the mid 1970s), the Very Large Array (VLA) and MERLIN telescopes (both in the early 1980s), jets were discovered to be associated with a large number of double radio sources. The development of Very Large Baseline Interpherometry (VLBI) showed that jets were also common among compact radio sources. In addition to extragalactic jets, there are many examples of jets and outflows that have been found within the Milky Way. The galactic jets span a great range of luminosities and collimation factors, from the optically visible jets and *lobes* associated with low-mass young stellar objects (YSOs), which are morphologically very similar to the classical radiogalaxies, to the poorly collimated and much less clearly defined *jets* associated with the Galactic Center and with various supernova remnants (Padman, Lasenby & Green 1991). VLA has allowed to detect in our galaxy the object SS433 (Abell & Margon 1979) and the *micro-quasars* GRS 1915+105 (Mirabel & Rodriguez 1994) and GRO J1655-40 (Tingay *et al.* 1995). In combination with VLBA (Very Large Baseline Array).

In the case of the diverse forms of extragalactic radio sources, the presence of jets is a manifestation of a more general phenomenon which is the nuclear activity in some galaxies. This nuclear activity characterizes the Active Galactic Nuclei (AGNs) which are among the most spectacular objects in the sky. They produce enormous luminosities (in some cases as much as 10^4 times the luminosity of a typical galaxy) in tiny volumes (probably $\gg 1$ pc^3; Krolik 1999). This radiation can emerge over a very broad range of frequencies (from infrared to gamma-rays). Their line spectra show in the optical and UV emission (and occasionally absorption) lines whose total flux is several percent to tens percent of the continuum flux, and whose widths suggest velocities ranging up to $\sim 10^4$ km s^{-1} (see *e.g.*, Krolik 1999).

The interpretation of the diverse forms of observed radio source structures has motivated the introduction of a classification scheme. Such classification scheme has changed as the number of observations has increased. Nowadays, the primary division among radio loud sources is the one that considers which part of the source has a large relative emission. Actually, the observations show that at low frequencies (*i.e.,* a few hundred MHz), in most instances the radio emission comes from a pair of extremely large lobes on opposite sides of the host galaxy. These lobes are often several hundred kpc in length and can be separated from the galaxy by a similar distance. The axis of the two lobes and the center of the galaxy generally lie along a common line. However, there are other radio loud objects in which, especially at higher frequencies (*i.e.,* several GHz), the region responsible for the bulk of emission is essentially unresolved on VLA (*i.e.,* 1 arcsecond scales), so that the source must be smaller than $\sim 20(D_A H_0/c)(h/0.75)^{-1}$ kpc, where D_A is the *angular diameter distance* (*i.e.,* distance at which the length between two objects whose angular separation is ϵ is given by $D_A\epsilon$), H_0 is the Hubble constant ($H_0 = 100h$ km s^{-1}) and h is the scale of the Hubble constant (usually $h = 0.65$). With this criterion, radio sources are divided into *lobe dominated* and *core dominated* (Muxlow & Garrington 1991). Each of these types have in its turn several subclasses. In the lobe dominated radio structures found in luminous spiral and elliptical galaxies are distinguishable three subtypes, associated to different classes of AGNs, *radio Seyfert galaxies*, *lobe-dominated radio galaxies* and *lobe-dominated radio-loud quasars.* Many Seyfert galaxies show S-shaped kpc scale radio structure (perhaps due to the disruption of the jet) and they are often less powerful emitters than elliptical galaxies. Usually, this difference is ascribed to the lower power output of the central nuclear engine and the dense rotating interstellar medium found in spiral discs (which difficults the plasma ejection through it). Some Seyferts however, do not contain any evident jet structure. Typical luminosities at 1 GHz ($P_{1\rm GHz}$) of this radio structures lie in the range $P_{1\rm GHz} \sim 10^{21} - 10^{25}$ W Hz^{-1}.

The properties of lobe-dominated radio galaxies are dependent on their luminosity. In fact there exits a critical luminosity ($P_{178\rm MHz} = 5 \times 10^{25}$ W Hz^{-1}) around which, structures seem to undergo an abrupt transition (Faranoff & Riley 1974) and, therefore they are conveniently classified as Fanaroff-Riley I (FR I) and II (FR II) if their luminosities are, respectively, below or above the former limit. FR I sources tend to have prominent smooth (*i.e.*, not knotty) continuous two-sided jets in antiparallel directions running into large-scale lobe structures (*plumes*) which are *edge-darkened*[1] and whose steepest radio spectra lie in the outermost extended regions furthest from the host galaxy. They exhibit linear polarization with electric vector normal to the jet, *i.e.*, the embedded magnetic field is aligned with the jet. The jets often contribute over 10% of the total power of the extended structure. A typical FR I source is associated to the radio galaxy 3C 449. FR II however, tend to have large-scale structures which are *edge-brightened* with bright outer hot spots and they are usually one-sided with a jet to counter-jet intensity ratio $> 4:1$. These jets are usually not smooth (*i.e.*, formed by a set of bright knots). The steepest radio spectra are found in the inner extended regions of the lobes or *bridges*. They show parallel polarization with a magnetic field perpendicular to the jet axis. The cores and jets in these structures usually contain $< 10\%$ of the total source luminosity which results in the non-detection of some cores. The opening angle of jets in FR II sources are smaller than those for FR I structures. Of course, the transition from FR I to FR II is not abrupt, and there is a special class of sources (*fat doubles*) which are among the weakest FR II sources (near the FR I/FR II luminosity limit), have a steeper spectrum than typical FR II, and are characterized by fatter lobes and almost no evidence for cores, jets or hot spots. The most characteristic example of FR II source is Cygnus A (3C 405).

The overall morphology of lobe-dominated radio sources is believed to be dominated by their interaction with the external medium (*e.g.*, Blandford & Rees 1974 –BR74, hereafter–). Actually, due to this interaction, it is possible that the path of the jet would be changed or even considerably bent. This is the case for *Narrow-Angle-Tail* (NAT) sources, *Wide-Angle-Tail* (WAT) sources, and *Steep spectrum core* sources. NATs are FR I type structures with bent two-sided (and almost symmetrical) jets running into an extended tail. They are usually located in clusters of galaxies where the host galaxy has a large proper motion with respect to the cluster

[1]Edge-darkened (see *e.g.*, Muxlow & Garrington 1991, or, Krolik 1999) means that the ratio of the total separation of the peaks of radio lobe emission to the source size (*i.e.*, the distance between the outermost detected parts of the lobes), is significantly less than unity. For FR I sources this ratio is less than 0.5, while for FR II sources the ratio is close to one.

and the radio structure is bent back by ram pressure from the hot external medium found in clusters (Begelman, Rees & Blandford 1979). The most well-known example of this class is NGC 1265. WATs sources were first classified as a new morphological class by Owen & Rudnick (1976). They are C-shaped structures formed by FR I disrupted plumes or tails with inner hot spots linked to the central components by jets. Jets seem to have physical properties similar to FR II type structures (quite knotty and with jet/counter-jet intensity ratios $> 4:1$). Although there are not too many observed structures of this type, they are often associated to optical dominant galaxies in rich clusters, and have total radio luminosities intermediate between NAT sources and typical FR IIs. An example of this structural type is 3C 465. Steep Spectrum Core sources are dominated by a kpc scale steep spectrum component associated with the nucleus of the parent object, surrounded by a diffuse low surface brightness halo. Objects of this class are also called *Core-Halo* sources, where "Core" states for the complete nuclear component rather than the compact flat spectrum feature within it. The best studied example of this structural type is the radio galaxy M 87.

The *lobe-dominated radio-loud quasars* are mainly found at high redshift and consist of very powerful radio extended structures surrounding some quasars. Their luminosity is above $P_{178\mathrm{MHz}} = 5 \times 10^{25}$ W Hz^{-1}, and display morphological features similar to FR II sources of equivalent luminosity. They have bright one-sided radio jets and cores with higher luminosities than those found in radio galaxies. The jets are knotty, one-sided (jet/counter-jet intensity ratios $> 4:1$) and with small opening angles. An example of this type of sources is 3C 179 (Shone, Porcas & Zensus 1985).

Core-dominated sources have very luminous cores and usually bright one-sided jets. VLBI studies (for which these objects are particularly appropriate because they have a very high core surface brightness) have pointed out that there is a continuity between the small and large-scale structures with a milliarcsecond scale one-sided jet (*i.e.*, $20(\theta/1\mathrm{mas})(D_A H_0/c)(h/0.75)^{-1}$, being θ the angular size) running into the outer arcsecond scale jet (kpc scale). Significant bending of the jet, specially near the core, is a common feature in these sources; for example 3C 273 bends by $\sim 20^o$ within the first 10 mas before extending continuously for 22 arcseconds (~ 40.7 kpc) from the core to beyond the limit of the optical jet (Whitney *et al.* 1971; Cohen *et* *al.* 1971). Knots in the VLBI jet are often observed to be moving away from the core with apparent *superluminal* speed. 3C 120 was one of the first four sources in which superluminal motion was detected on the scale of pc (Seielstad *et al.* 1979; Walker, Benson & Unwin 1987) to tens of pc (Benson *et al.* 1988; Walker 1997; Muxlow & Wilkinson, 1991; Gómez *et al.* 1998, etc.). The most complete set of epochs and high resolution VLBA observations has been undertaken by Gómez, Marsher & Alberdi (1999). In this work and in Gómez *et al.* (1998), up to ten superluminal components, with velocities between 2.3 and 5.4 $h^{-1}c$, are shown. In addition to the core and jet, VLA images show a low surface brightness extended component that is often found on the opposite side to the jet and, in some cases, this whole triple structure is embedded in a very low surface brightness amorphous halo like in the case of 1642+690 (Browne 1987). The jet properties are broadly similar to those found in lobe-dominated quasars, but are of higher luminosity and show a greater degree of bending.

Finally, there exist a morphological class (which is a remnant of the poor resolved observations with the Cambridge 5 km telescope) named *compact steep-spectrum* sources (Fanty *et al.* 1990). Most of them resembled miniature extended sources. Detailed VLA and VLBI observations conclude that these radio structures are of galactic or subgalactic dimensions (*i.e.*, linear sizes $\sim 1 - 10$ kpc) and have a wide variety of morphologies (some are like doubles, others appear as core-jet structures, and in a number of cases they are so extremely distorted that cannot be easily classified). Fanty *et al.* (1985) have shown that there is a clear division between quasars and radio galaxies in this class: the quasars are generally core-jet or complex while the galaxies are doubles. Furthermore, some authors (*e.g.*, Phillips & Mutel 1980) have claimed that the double structures represent the young progenitors of classical double radio sources. Others have argued that these sources are a separate class of intrinsically small objects where the jets encounter great difficulty in escaping from the inner regions of the host galaxy or quasar (Fanti & Fanti, 1986).

3.1.2. The standard model

We have stated above which is the gross classification of the enormous set of observations of radio sources. Now we focus on the models that allow us to understand such observations. There exists a unifying interpretation consisting in that our view of a radio source is influenced by our relative orientation with respect to the source axis (regardless of its luminosity). In the standard model (BR74; Scheuer 1974) jets are considered as continuous channels of matter highly collimated, supersonic and very stable. Additionally, following Blandford & Königl (1979) the superluminal motions and the jet asymmetries in compact sources are explained by assuming that both the jet and the counter-jet propagate with relativistic speeds at a small angle to the line of sight towards the observer. The relativistic Doppler beaming of the emission in the direction of motion can account for the observed asymmetry in the luminosity of the jets. Additionally, the component of the velocity over the plane of the sky may exceed the light speed due to a pure kinematic relativistic effect giving rise to apparent superluminal velocities[2]. Assuming that this interpretation of the superluminal motion is true and taking into account the relativistic beaming, bulk flow motions with Lorentz factors as large as 20 may be assigned to many compact radio jets.

The mechanism for the jet formation and collimation is still a challenge, mainly because we have not detailed enough observations (*i.e.,* with sufficient resolution) because the most detailed high-frequency VLBI observations of nearby radio sources can resolve at most the compact radio cores with linear resolutions of ≥ 100 mpc (Blandford 1990) [3] while the Schwarzschild radius ($R_s = GM/c^2$) of a $10^9 M_\odot$ galactic BH is ~ 10 μpc. Consistently, our theoretical view of the jet formation must be mainly constrained by the fact that many jets are well collimated by the time they have propagated to a distance $\leq$ 1pc from the nucleus (Blandford 1990; Junor & Biretta 1995). Considering this element, many mechanisms have been proposed, all

[2]The apparent velocity is define as $v_{\rm app} = v \sin\Psi/(1 - v\cos\Psi)$, Ψ and v being the angle that forms the source respect to the line of sight and the velocity, respectively.

[3]Nowadays, within the project VLBI Space Observatory Program (VSOP), the angular resolution is higher allowing for linear resolution of $\sim 0.1 - 1$ pc even in distant sources like S5 0836+710 ($z = 2.17$; Lovanov *et al.* 1998).

of which present some difficulties (Begelman, Blandford & Rees, 1984) and, additionally, there is a wide variety in the observed properties of jets, so there may be a variety of jet collimation mechanisms.

Our common wisdom about AGNs establish the following *anatomy* for the innermost (*i.e.*, ≤ 100 mpc) part of the nuclei:

- **10 mpc scale.** It is usually accepted that the power that feeds the ejection is the matter which is accreted onto a black hole (BH) coming from an accretion disk. The morphology and dynamics of this accretion disk is different depending on the distance to the BH. At this scale, the disk may be *ionized*, being the evidence for this the optical continuum in quasars (if it is true that this continuum is mainly thermal in origin). A relativistic jet is still formed which emits due to synchrotron and inverse Compton. Moreover, a toroidal magnetic field may be the responsible for jet collimation.

- **1 mpc scale.** At this scale, the temperature is higher and may produce UV radiation. The disk would be *radiation pressure* and *Thomson opacity* dominated. The poloidal component of the magnetic field presumably helps to extract matter from the accretion disk and accelerate it at velocities of $\sim 0.1c$.

- **100 μpc scale.** Within ten times of the radius of the BH, the nature of the gas flow is quite controversial, but with complete certainty the effects of *General Relativity* must determinate their characteristics. Observation of highly variable X-ray emission from Seyfert galaxies imply that the X-rays originate from this region (produced by electron–positron (e^-e^+) annihilation into the plasma that forms the relativistic jet).

- **10 μpc scale.** This is the typical BH scale and perhaps also its magnetosphere. The mass of the BH dictates a characteristic length and luminosity scale for nuclear activity.

The collimation of such matter emissions can be due to the combined action of toroidal magnetic fields, radiation pressure, purely thermal pressure and other not yet understood processes. In the following paragraphs we will summarize the main issues that have been pointed out in order to explain the jet collimation up to ~ 1 pc (for more details see *e.g.*, Kembhavi & Narlikar 1999; Krolik 1999; or Blandford 1990).

The first force one might look to in order to drive outflows is ordinary gas pressure gradients. In the original scheme suggested by BR74, two twin antiparallel channels propagate in opposite directions from the nucleus. The jets, assumed to be made up of ultrarelativistic plasma, are subsonic close to the nucleus, but pass through a nozzle (*de Laval nozzle*) where the cross-sectional area is a minimum, and the flow is trans-sonic. Beyond the nozzle the flow is supersonic, and though the cross-sectional area increases, the angle which is subtended at the nucleus decreases, and well-collimated jets could be produced. However, even allowing for the reduced collimation caused by internal dissipation, entrainment, etc., this mechanism does not seem capable of creating well-collimated jets. The reason is that VLBI observations require that the collimation has to be produced on a scale $\lesssim$1 pc, where the gas pressure and density required would have to be very large that the consequent X-ray emission would easily exceed the observed upper limits for powerful sources. This collimation model can therefore work only for jets of low power $\lesssim 10^{43}$erg sec^{-1}.

Another possibility for jet collimation are the radiation forces. Such forces may be important in powerful sources (like quasars) which would be radiating very close to their Eddington limits. Then the pressure of radiation acting on $e^{-}e^{+}$ pairs may be sufficient to overcome gravity along certain directions. This would happen in the funnels formed by a radiation-pressure supported torus orbiting around a BH. The most fundamental problem of this model is that once the flow reaches mildly relativistic speeds[4] (much less than those usually invoked to account for superluminal motion), a medley of effects make further acceleration inefficient, while any isotropic radiation acts as a source of drag[5] (Phinney 1987). This radiative acceleration model may not apply to sources which are observed to radiate at sub-Eddington rates. Moreover, a theoretical complication of the model is that radiation-supported tori could not be dynamically stable, which puts in question their long term existence.

[4]Lorentz factors $\lesssim$3 (for a pair plasma) or smaller (for a plasma of electrons and ions).

[5]This radiation may drag the well collimated fluid from its outflowing direction, thus, loosing directionality and collimation.

A third possibility arises if magnetic forces are an important ingredient. These models are mainly based on thin magnetized accretion disks. Collimation seems to be a generic feature of hydromagnetic winds, the reason for this tendency being that one expects the footpoints of magnetic field lines to be fixed to the matter of the accretion disk. The field lines will then rotate with the orbital frequencies of their footpoints, creating a toroidal magnetic field even if there was none to begin with. This toroidal component has an associated *hoop* stress which can act to collimate the poloidal flow of the plasma. As the flows are centrifugally driven and magnetically confined, the gas pressure is not very important except, perhaps, close to the disk. In this magnetohydrodynamic (MHD) flows, there are three critical points, along a flow line, at which the gas becomes sonic (corresponding to the three types of wave modes which exist in MHD: fast, Alfvén and slow waves). After the field passes through the third point, the magnetic field becomes mostly toroidal, and the magnetic energy and angular momentum fluxes are typically half converted into mechanical energy and angular momentum. In the process the jets become collimated, whether they are relativistic or non-relativistic. In this models there is a correlation between the accretion rate and the speed of jets on the pc scale, so that quasar jets have highly relativistic speeds while jets in FR I galaxies may be non-relativistic (Camenzind 1993). A theoretical difficulty with this explanation for AGN jets is that magnetically collimated plasma is unstable, particularly to non-axisymmetric perturbations.

Having summarized in the previous paragraphs the fundamental theories that try to explain the mechanisms of jet formation and collimation, it is necessary to remark that only a limited progress has been made in understanding jet physics, because of the lack of detailed structural information on the very small spatial scales on which the jets are produced, as well as the complexity of the physical processes involved in the production and collimation. However, on bigger scales (from $\gtrsim$10 mpc to ~ 1 Mpc) a very detailed set of observations has been made in a large number of AGNs. This wide sample of observations has allow us to understand that powerful sources are supposed to comprise a core, and two jets which feed a pair of radio-emitting lobes. The radio-emitting electrons are supposed to be convected outward along the jet with relativistic speed so that they beam their emission along their directions of motion (due to the *relativistic beaming*). Most of the compact radio sources are intrinsically weaker and their compactness is mainly a projection effect due to that they are beamed in our direction so that their compact jet emission outshines the unbeamed emission from the lobes. In addition to this, from the observations, it is possible to infer a characteristic *anatomy* of the observable parts of the jets, in which two main regions are distinguishable in terms of the distance to their origin: the *parsec* and *kiloparsec* scales.[6]

a) the *parsec scale (100 mpc – 100 pc)*:

- *Observational facts*: the jet emits at radio frequencies due to synchrotron and inverse Compton processes, and it is observed using VLBI imaging. It displays a high collimation and its morphology is characterized by a bright spot at the jet end and a series of components (usually preceded by outbursts in emission at radio wavelengths) which separate from the core, sometimes at superluminal speeds. Many parsec scale jets show intraday variability of the radio flux, excess in brightness temperatures and one-sidedness. Between 1 and 10 pc the *broad emission lines* seem to be produced. These are observed in about 12% of all quasars (Weymann *et al.* 1991). At about 10 pc the BH's gravity may begin to dominate the stellar distribution. In some galaxies the stellar velocity rises with decreasing radius. The jets may exhibit structure reflecting this change in gravitational potential. The *narrow emission lines* are detected at scales ~ 100 pc.
- *Theoretical interpretation*: the jet material moves at small angles to the line of sight with bulk Lorentz factors $W \simeq 10(H_0 h)^{-1}$ (Ghisellini *et al.* 1993), or maybe larger ($W \simeq 30 - 100$) if the intraday variability is intrinsic and a result of incoherent synchrotron radiation (Begelman, Rees & Sikora 1994). The moving components are interpreted in the shock-in-jet model as traveling shock waves (Marscher & Gear 1985; Hughes, Aller & Aller 1989; Gómez, Alberdi & Marcaide, 1994, Gómez *et al.* 1994). A worthy byproduct of this model is the explanation of the complex

[6] This division follows in distance to the previous scale (the *subparsec scale*) that we have explained previously.

multifrequency brightness and polarization variations in blazars. The width of the emission lines is interpreted in terms of the local velocity of the clouds where the absorption is produced. For the broad lines, a Doppler spreading interpretation ascribes flow velocities up to 60000 km sec^{-1} in the gas which is within the quasar itself, relative to the emission redshift. The narrow emission lines are generated in clouds which are farther from the AGN center.

b) the *kiloparsec scale (1 kp – 1 Mpc)*:

- *Observational facts*: $\sim$ 1 kp and $\sim$ 10 kpc are the typical sizes of the galactic center nucleus, and the host galaxies, respectively. At this scale there exist a dichotomy between FR I and FR II sources whose basis seems to be the source power. Between 100 kpc and 1 Mpc the radio jets are quite common, and extended radio lobes (which eventually may contain bright host spots) can be found. The overall shapes of the jets are sensitive to the galactic and circumgalactic environment (for example, NAT and WAT sources have their characteristic morphology due to the presence of high peculiar velocities in rich clusters of galaxies). Evidences of mildly relativistic jet speeds ($\sim 0.6-0.8$c, for the double–lobed quasar 3C 179; Akujor 1992) well outside the galaxy have been found, like *e.g.,* flux asymmetries between jets and counter-jets (Bridle *et al.* 1994) and superluminal motions at kpc scales (*e.g.,* in 1928+738, Hummel *et al.* 1992, in 1055+201, 1830+285, 2209+080, Hooimeyer *et al.* 1992).
- *Theoretical interpretation*: morphologies of FR I sources are the result of a deceleration from relativistic to non-relativistic speeds (Bicknell 1996; Laing 1996). FR I sources are mostly supposed to be moving with subrelativistic and probably no more than transonic speeds (Bicknell 1984; Begelman, Blandford & Rees, 1984). Their jets are therefore visible from both sides of the central galaxy (because small relativistic velocities imply small relativistic beaming). The transonic speeds on kpc are explained in terms of a slower shear layer that surrounds the inner core of the jet (for example, in M 87, Biretta & Owen, 1990 or Biretta, Zhou & Owen, 1995, have detected a shear layer with Lorentz factor ≤ 2). The existence of this

layer has been pointed out by several authors both theoretically (Laing 1996; Komissarov 1990) and observationally (*e.g.*, Swain, Bridle & Baum 1998; Biretta, Zhou & Owen 1995), and has been buttressed by numerical simulations (like *e.g.*, Aloy *et al.* 1999b –3D RHD–; Hardee & Rosen, 1999 –3D MHD–). In the most powerful sources (FR II and quasars), the jet–counter-jet asymmetries are understood as the result the enhancement of the jet emission due to the relativistic beaming while the counter-jet is outshined. The mechanism by which the relativistic flows inferred from radio jets at pc scales extend to kpc scales is still an unresolved question. However, the named transition and the ulterior propagation of jets needs of an efficient mechanism that stabilizes the possible developing of (magneto-)hydrodynamical instabilities (mainly Kelvin-Helmholtz instabilities).

3.1.3. Numerical simulations

The study of the jet phenomenon using numerical simulations has become an important tool to understand the nature of the jets along with theory and observations. In order to simulate astrophysical jets a *fluid-like* approximation is usually made, considering the intergalactic medium (IGM) and the jets themselves as continuous mediums in which the hydrodynamic (HD) equations hold. The validity of this approximation is justified because of the presence of micro-Gauss magnetic fields which provide the collisional coupling of the plasma (and hence, diminishing the collisional mean free path of the jet plasma) and, moreover, Begelman, Blandford & Rees (1984) stated that in extragalactic jets the Larmor radii and Debye lengths of positrons (or protons) and electrons are several orders of magnitude smaller that the jet widths.

In BR74 was made the first one-dimensional Newtonian study of jets in order to analyze the behavior of a steady flux in pressure equilibrium with the IGM. From this work is concluded that the head of the jet must end into a discontinuity that has a supersonic velocity which, in its turn, produces a *bow shock* behind the contact discontinuity. In addition, the authors suggest that a movement parallel but with opposite sense to the jet ought to appear (the *backflow*) giving rise to the formation of a *cocoon* than surrounds the beam.

The simulations performed by Rayburn (1977) and, remarkably, by Norman *et al.* (1982) allowed for the verification of the jet model of BR74 and Scheuer (1974). Similarly to the observations, the evolution of numerical complexity of the simulations has grown in parallel to the improvement of computers and computational techniques. The main goals of the numerical work in the late 1970s and 1980s have been the simulation of classical (Newtonian) jets in three spatial dimensions and the consideration of dynamically important magnetic fields (in the framework of the ideal MHD). Classical HD simulations provided us a new insight into the structures observed in many VLA radio images (Norman *et al.* 1982) while MHD simulations showed the importance of toroidal magnetic fields for the confinement of jets (Clarke, Norman & Burns 1989; Lind *et al.* 1989; Kössl, Müller & Hillebrandt 1990; Appl & Camenzind 1992). The stability and mixing properties of high Mach number jets have been studied by means of HD numerical simulations in Bodo *et al.* (1995) (2D slab symmetry) or Bodo *et al.* (1998) (3D). The stability of MHD jets using an artificial viscosity scheme (see Chapter 2, §2.1) was explored by Hardee & Norman (1988), Norman & Hardee (1988) or Hardee *et al.* (1992) (2D slab symmetry), and Hardee, Clarke & Howell (1995) or Rosen *et al.* (1999) (3D jets). Numerical simulations have been used to investigate the confinement properties of overpressured cocoons in hypersonic jets (see Begelman & Cioffi, 1989) by Loken *et al.* (1992). In order to explain the observed morphologies in NAT and WAT sources, the interaction with the IGM has been included in some simulations like *e.g.,* Balsara & Norman (1992) –3D simulations of NAT jets with a cross wind–, Norman, Burns & Sulkanen (1988) and Loken *et al.* (1995) –2D and 3D simulations of WAT sources in which the ambient gradients play a crucial rôle in the morphology–.

In the late 1980s and during the 1990s the dynamical and morphological properties of relativistic jets have been investigated by means of relativistic simulations. The classical numerical techniques (*e.g.,* Wilson 1979) failed to describe accurately complex fluids with strong shocks, large Lorentz factors or were impractical in multi-dimensions (see Norman & Winkler 1986). Such drawback restricted the relativistic simulations to the stationary regime (Wilson 1987; Daly & Marscher 1988; Dubal

& Pantano 1993; Bowman 1994). Thereat, in order to fix these problems and to be able of undertaking relativistic simulations it was necessary to write the equations of RHD as a system of conservation laws, and employ new numerical methods exploiting the hyperbolic and conservative character of RHD equations (see *e.g.*, Martí *et al.* 1991; Marquina *et al.* 1992; Schneider *et al.* 1993; Eulderink & Mellema 1995; Martí & Müller 1996). The new treatment has allowed to produce axisymmetric time-dependent relativistic hydrodynamical simulations (Duncan & Hughes 1994; Eulderink & Mellema 1994; Martí *et al.* 1994, 1995, 1997; Komissarov & Falle 1998; Rosen *et al.* 1999). These simulations allowed to conclude that the main relativistic effect is that both the internal energy and the Lorentz factor increase the effective inertial mass of the beam which directly contributes to enhance the stability of relativistic jets compared to their classical equivalents with *similar* parameterizations.[7]

Relativistic MHD simulations in 2D (van Putten 1993, 1996 –using pseudo-spectral techniques–; Koide, Nishikawa & Muttel 1996; Koide 1997) and 3D (Nishikawa *et al.* 1997, 1998) have been another step forward in the understanding of the jet phenomenon. A remarkable difference between our HRSC methods and the TVD methods used by the Japanese group is that Koide and collaborators code, instead of using fluxes obtained by solving Riemann problems at zone interfaces, rely on the addition of nonlinear dissipation terms to their Lax–Wendroff scheme to stabilize the code across discontinuities. This stabilization method was originally proposed by Davis (1984), who applied it successfully to the equations of classical HD. The method is robust and simple as no detailed characteristic information is needed. Koide and collaborators did simulate the evolution of the jet only for a very brief period of time. This fact and the coarse grid zoning used in their simulations, prevented them from studying genuine 3D effects in relativistic jets in any detail. On the other hand, the relative smallness of the beam flow Lorentz factor (4.56, beam speed ≈ 0.98) assumed in their simulations does not allow for a comparison with Riemann-solver-based HRSC methods in the ultrarelativistic limit.

[7]The direct comparison between classical and relativistic jets is not possible, because the beam velocity is an extra parameter (in the relativistic case) which cannot exceed the light speed. Some issues in the method for this comparison have been outlined by Komissarov (1996), who suggested to establish equivalents considering jets with the same *useful* power (the energy flux) or the same thrust (the momentum flux) at the jet inlet.

Finally, only very recently, within the framework of General Relativity, general relativistic MHD 2D axisymmetric simulations of jet formation near a rotating K-err BH (assuming a fixed Kerr background metric) have been performed by Koide *et al.* (1999a,b). However, their results are still preliminar, because in Koide *et al.* (1999a) it is said that a jet is formed with a maximum velocity $0.93c$ ($W = 2.7$), and for a non-rotating Schwarzschild black hole, the maximum outflow velocity is less than $0.6c$ for initial magnetospheric conditions similar to those of the Kerr black hole case. In Koide *et al.* (1999b), nevertheless, the maximum velocities obtained are $0.4c$ (counter-rotating disk) and $0.3c$ (co-rotating disk), and the results in the Schwarzschild case are very similar to the co-rotating case.

3.2. 3D Hydrodynamical simulations of large–scale jets

As stated in Chapter 2, one of the applications of GENESIS is the study of large–scale jets. In order to begin such a research in three spatial dimensions we have first considered a 3D axisymmetric reference model consisting of a relativistic jet propagating through an homogeneous atmosphere. Of course, this model could be calculated with a two-dimensional code using cylindrical coordinates. However, it will be taken as a calibration of the results in 3D (compared with the same model in 2D), and additionally it will be used as a reference model in order to compare with other 3D models which result from a slight perturbation of the axisymmetric one.

3.2.1. An axisymmetric jet in 3D

We have considered a 3D model corresponding to model C2 of Martí *et al.* (1997), which is characterized by a beam-to-external proper rest-mass density ratio $\eta = 0.01$, a beam Mach number $\mathcal{M}_b = 6.0$, and a beam flow speed $v_b = 0.99c$ (beam Lorentz factor $W_b \approx 7.09$). An ideal gas equation of state with an adiabatic exponent

$\gamma = 5/3$ is assumed to describe both the jet matter and the ambient gas.[8] The beam is in pressure equilibrium with the ambient medium which fills a Cartesian domain (X,Y,Z) with a size of $15R_b \times 15R_b \times 75R_b$ ($120 \times 120 \times 600$ computational cells), where R_b is the beam radius. The jet is injected at $z = 0$ in the direction of the positive z-axis through a circular nozzle defined by $x^2 + y^2 \leq R_b^2$, and is in pressure equilibrium with the ambient medium. Outflow boundary conditions are imposed everywhere except at the plane $z = 0$, where injection is assumed through the nozzle and the rest of the plane has a reflecting boundary. Two different spatial resolutions with 4 and 8 zones per beam radius were used in our calculations (Figs. 3.1, 3.2). Simulations are typically performed with 16 processors and need about ten thousand time iterations.

Given that our relativistic, highly-supersonic models are dimensionless, we can scale the beam kinetic power, P_j, of the jets according to

$$P_j = 3.5\,10^{46} \left(\frac{R_b}{100\,\mathrm{pc}}\right)^2 \left(\frac{\rho_a}{10^{-26}\,\mathrm{g\,cm^{-3}}}\right) \mathrm{erg\,s^{-1}} \,, \tag{3.1}$$

which for typical values of the beam radius and the ambient density is that of a powerful jet (Rawlings & Saunders 1991, Daly 1995).

In Martí et al. (1997) the simulation was performed in cylindrical coordinates assuming axial symmetry. The spatial resolution was 20 zones per beam radius both in the axial and radial directions. It is well known that the propagation of a supersonic jet is governed by the interaction of jet matter with the ambient medium, which produces a bow shock in the ambient medium and an envelope surrounding the central beam (the *cocoon*, in BR74). The cocoon contains jet material deflected backward at the head of the jet. In the case of highly supersonic jets, discussed in Martí et al. (1997), extensive, overpressured cocoons are formed with large vortices of jet matter propagating down the cocoon/ambient medium interface. The vortices are the result of Kelvin–Helmholtz instabilities at the interface between the jet and the shocked ambient medium. The interaction of these vortices with the central beam causes internal shocks inside the beam. These, in turn, affect the advance

---

[8] According to Martí *et al.* (1997), high Mach numbers correspond to flows with small specific internal energies and, consistently we have chosen for this model a nonrelativistic value for γ.

speed of the jet making it highly non–stationary. The propagation speed of the jet can be estimated from the momentum transfer between the jet and the external medium assuming a one dimensional flow. For model C2 one obtains an advance speed equal to $0.42c$ (which agrees with the 1D estimate for the head of the jet speed[9]), whereas the 2D hydrodynamic simulation presented in Martí et al. (1997) gives a mean jet advance speed of $0.37c$.

The four panels in Figs. 3.1, 3.2 display, from top to bottom, the logarithm of the proper rest-mass density, pressure and specific internal energy and flow Lorentz factor in the plane $x = 0$ at $t = 160\, R_b/c$, when the jet has propagated about $75\, R_b$. The analysis of cross sections of the grid perpendicular to the the jet's direction of propagation (not shown here) reveals acceptable symmetry of the numerical simulation, *i.e.,* both the SLS and the SCS properties are maintained (see §2.3.10).

The gross morphological and dynamical properties of highly relativistic jets as inferred from our 3D simulations are qualitatively similar to those established in earlier 2D simulations. An extensive, overpressured cocoon with pressure about 20 times that in the beam at the injection point is found surrounding the jet. The pressure and density at the head of the jet in the model with 8 zones/R_b are a factor of 2 larger and 1.3 smaller, respectively, than in the 2D calculation. For the model with 4 zones/R_b these factors are 1 and 1.3, respectively. In contrast with the model with 4 zones/R_b, in which the propagation speed coincides with the 1D estimate, the larger pressure at the head of the jet in the model with 8 zones/R_b causes it to propagate through the ambient medium at a larger speed in the 3D calculation ($0.47c$ instead of $0.42c$ for the 1D estimate and $0.37c$ for the 2D simulation) producing a narrower profile of the bow shock near the head. In all the simulations, the supersonic beam displays rich internal structure with oblique shocks effectively decelerating the flow in the beam from a Lorentz factor equal to 7 at the injection point down to a value of about 4 near the head. Whereas gross morphological properties are qualitatively similar in all three simulations, finer jet details (e.g., number, size, position and development of turbulent vortices in the cocoon) do not agree. However, it has been pointed out before that the fine structure

[9] $v_{1D} = \sqrt{\eta_R^*}/(1+\sqrt{\eta_R^*})v_b$, with $\eta_R^* = (\rho_b h_b)/(\rho_m h_m)W_b^2$, ρ_m and h_m being the density and the enthalpy of the external medium (for more details see, *e.g.,* Martí *et al.* 1997)

is highly dependent on the numerical grid resolution (see, *e.g.*, Kössl & Müller 1988).

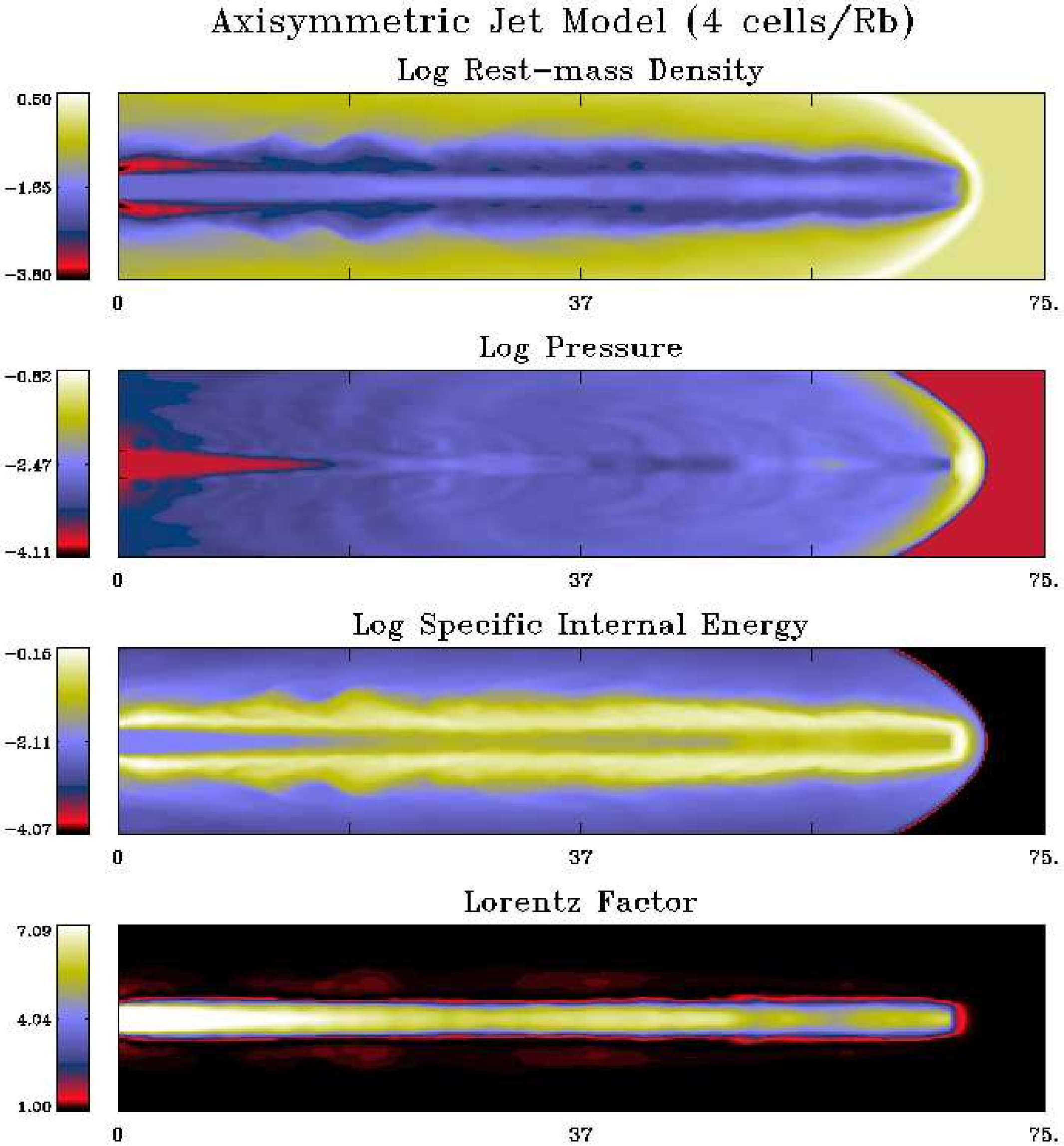

Fig. 3.1.— Snapshots (from top to bottom) of the proper rest–mass density distribution, pressure, specific internal energy (all on a logarithmic scale) and Lorentz factor of the relativistic jet model discussed in the text ($v_b = 0.99c$, $\mathcal{M}_b = 6.0$, $\eta = 0.01$, $\gamma = 5/3$) after 160 units of time. The resolution is 4 zones/R_b.

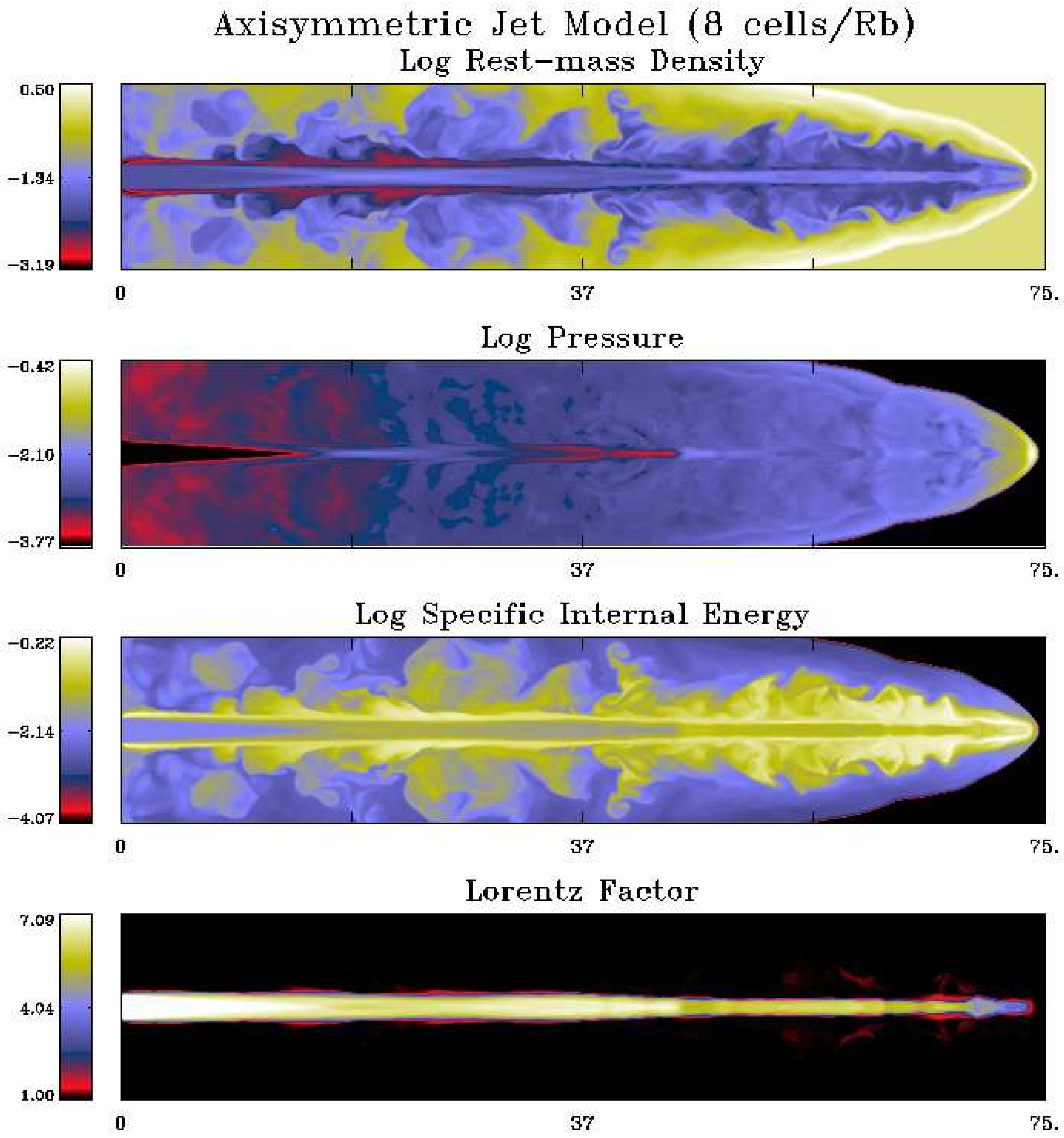

Fig. 3.2.— Same as Fig. 3.1 but with a resolution of 8 zones/R_b.

In the model with 4 zones/R_b (see Fig. 3.1), the material deflected at the head of the jet forms a thick, stable overpressured cocoon surrounding the beam up to the nozzle. Due to the small resolution only large vortices develop in the cocoon/external medium surface which grow slowly. A turbulent cocoon with smaller vortices growing at a faster rate (much more similar to the one got in the 2D cylindrical model) are obtained by doubling the resolution (compare, *e.g.*, the proper rest–mass density panels in Figs. 3.1, 3.2). There exists a layer of high energy around the beam, which is wider an more energetic in the model with the worst resolution. The layer widens from the nozzle to the hot spot.

3.2.2. General considerations

The calculations in the following sections have been performed with an updated version of the code GENESIS (see Chapter 2), which includes an additional conservation equation for the beam-to-external density fraction to distinguish between beam and external medium fluids. The beam material is injected with a beam mass fraction $f = 1$, and the computational domain is initially filled with an external medium ($f = 0$).

First of all, we will discus in detail the simulation showed in Aloy *et al.* (1999b). In this memory such simulation corresponds to the model n50p01 (see Table 3.1). This model is slightly perturbed compared with the axisymmetric case, but it displays all of the specific 3D morphodynamical features that are common to the remaining simulations. After that we will compare with other perturbed 3D models. Aloy *et al.* (1999b) reported on a high-resolution 3D simulation of a relativistic jet with the largest beam flow Lorentz factor performed up to now (7.09), the largest resolution (8 cells per beam radius), and covering the longest time evolution (75 normalized time units; a normalized time unit is defined as the time needed for the jet to cross a unit length; see Massaglia, Bodo & Ferrari 1996). These facts together with the high performance of our hydrodynamic code allowed us to study the morphology and dynamics of 3D relativistic jets for the first time. Here, we consider a wider sample of models to study such features in more detail.

The evolution of the jet was simulated up to $T \approx 150 R_b/c$, when the head of the jet is about to leave the grid. The mean jet propagation speed is $v_h \approx 0.5c$, while $v_{1D} \approx 0.42c$, *i.e.*, our simulations are still within the 1D phase (see Martí, Müller & Ibáñez 1998). The scaled final time $T \approx 4.6\,10^4\ (R_b/100\,\mathrm{pc})$ yr is about two orders of magnitude smaller than the estimated ages of powerful jets. It is expected that in the long term evolution (Martí, Müller & Ibáñez 1998) both the jet advance speed and the jet's head pressure $p_h \approx 2.6\,10^{-7}(\rho_a/10^{-26}\,\mathrm{g\,cm^{-3}})\,\mathrm{dyn\,cm^{-2}}$ decrease until they reach realistic values ($v_h \approx 0.05c$, $p_h \lesssim 10^{-8}\,\mathrm{dyn\,cm^{-2}}$; Daly 1995). Hence, our simulations cannot describe the long term evolution of these sources and conclusions should be extrapolated cautiously.

In order to induce three-dimensional effects, non–axisymmetry was imposed by means of a helical velocity perturbation at the nozzle given by

$$v_b^x = \zeta_p v_b \cos\left(\frac{2\pi t}{\tau_p}\right),\ v_b^y = \zeta_p v_b \sin\left(\frac{2\pi t}{\tau_p}\right),\ v_b^z = v_b\sqrt{1-\zeta_p^2}, \qquad (3.2)$$

where ζ_p is the ratio of the toroidal to total velocity and τ_p the perturbation period (*i.e.*, $\tau_p = T/n$, n being the number of cycles completed during the whole simulation). This velocity field causes a differential rotation of the beam, the fluid near the axis rotating faster. The wavelength of the perturbation, λ_p, is obtained from the expression

$$\lambda_p = v_b^z \tau_p \approx \frac{v_b}{v_h}\frac{L}{n}, \qquad (3.3)$$

where L is the axial dimension of the grid (in our simulations, 75 R_b). Note that the perturbation is chosen such that it does not change the velocity modulus, *i.e.*, it preserves mass, momentum and energy flux of the beam. Table 3.1 collects the perturbation parameters considered in our study. The chosen parameters try to cover different perturbation types and all their possible combinations. This is the reason to include *high* ($n = 50$) and *low* ($n = 15$) frequency modes and *small* ($\zeta_p = 0.01$) and *medium* ($\zeta_p = 0.05$) amplitude perturbations.

3.2.3. Morphology and dynamics of 3D relativistic jets

Figure 3.3 shows various quantities of the model n50p01 in the plane $y = 0$ at the end of the simulation. Two values of the beam mass fraction are marked with white contour levels. The beam structure is dominated by the imposed helical

Model	n	ζ_p	τ_p	λ_p
n15p01	15	0.01	10	11.8
n15p05	15	0.05	10	11.8
n50p01	50	0.01	3	3.5
n50p05	50	0.05	3	3.5

Table 3.1: Perturbation parameters of the numerical simulations and expected values of the perturbation wavelength.

pattern with a characteristic wavelength of $\approx 3.0R_b$ (to be compared with the value $\lambda = 3.5R_b$ expected from Eq. (3.3)) and an amplitude of $\approx 0.2R_b$.

3.2.3.1. Cocoon

The overall jet's morphology is characterized by the presence of a highly turbulent, subsonic, nearly asymmetric cocoon. The pressure distribution outside the beam is quite homogeneous giving rise to a symmetric bow shock (Figs. 3.3b). As in the classical case (Norman 1996), relativistic 3D simulations show less ordered structures in the cocoon than in the 2D axisymmetric calculations (where strongly structured circular vortices are present). As seen from the beam mass fraction levels, the cocoon remains quite thin ($\sim 2R_b - 3R_b$).

The flow field outside the beam shows that the high velocity backflow is restricted to a small region in the vicinity of the hot spot (Fig. 3.3e), the largest backflow velocities ($\sim 0.5c$) being significantly smaller than in 2D models. The flow annulus with high Lorentz factor found in axisymmetric simulations (see flow patterns in Martí *et al.* 1996) is also present, but it is restricted to a thin layer around the beam and possesses sub-relativistic speeds ($\sim 0.25c$). The smallness of the backflow velocities in the cocoon do not support the possibility of having relativistic beaming of the emitting material moving backwards in the counter-jet. The unrealistically large speed of the hot spot (see Sect. 3.2.3.4) prevents fast backflows because the

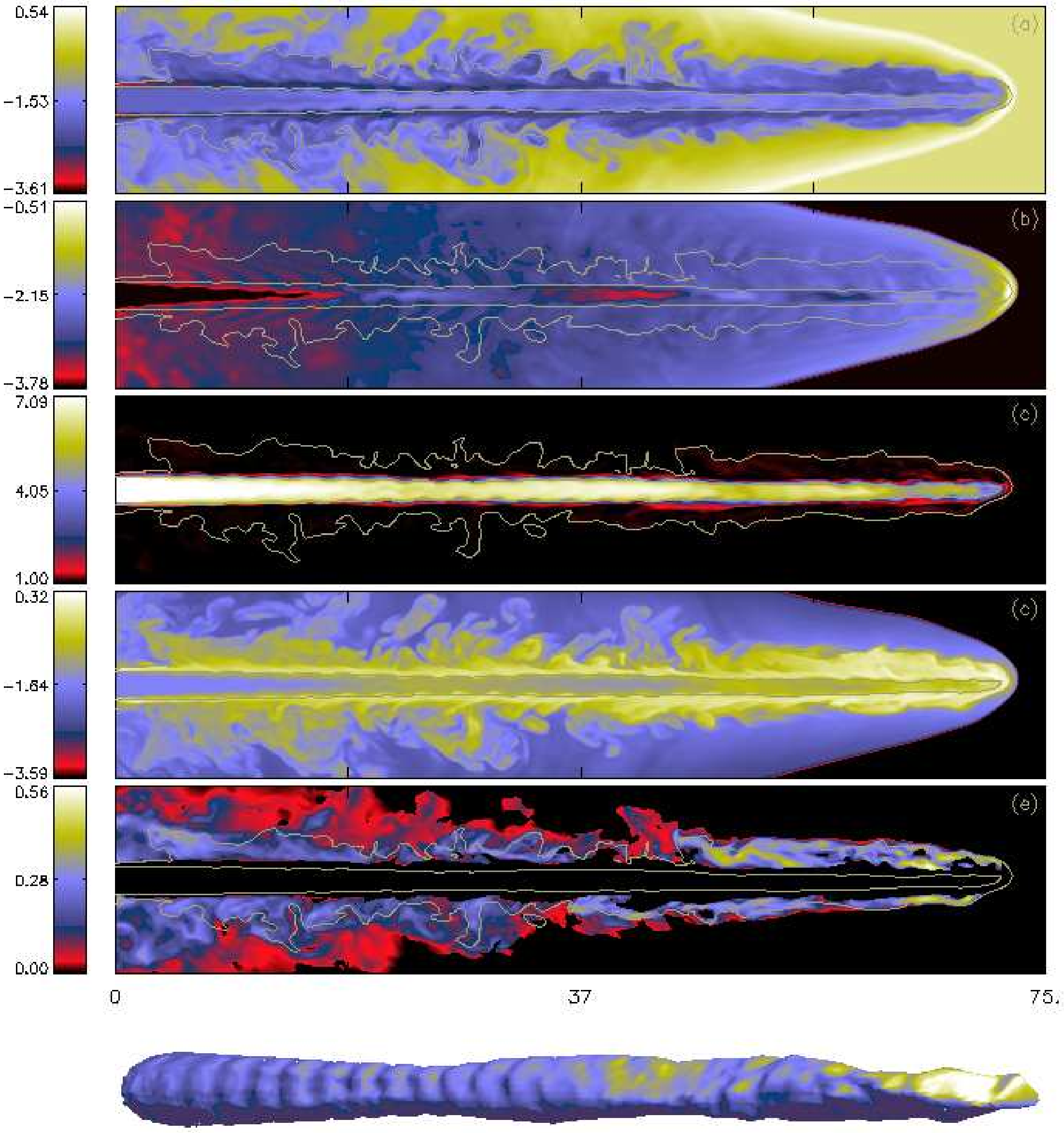

Fig. 3.3.— Rest-mass density, pressure, flow Lorentz factor, specific internal energy and backflow velocity distributions (from top to bottom) of the model n50p01 in the plane $y = 0$ at the end of the simulation. White contour levels appearing in each frame correspond to values 0.95 (inner contour; representative of the beam) and 0.05 (representative of the cocoon/shocked external medium interface) of the beam mass fraction. The bottom panel displays the isosurface of beam mass fraction equal to 0.95.

material efficiently pushes the terminal contact discontinuity and, therefore, only a small fraction of the beam fluid is deflected backwards. However, as the hot spot pressure is larger too, it favors the acceleration of the rear-going beam material.

3.2.3.2. Beam and hot spot

Within the beam the perturbation pattern is superimposed to the conical shocks at about 26 and 50 R_b. The beam does not exhibit the strong perturbations (deflection, twisting, flattening or even filamentation) found by other authors in the classical case (Norman (1996) for 3D HD jets; Hardee (1996) for 3D MHD jets). This can be taken as a sign of stability, although it can be argued that our simulation has not evolved far enough. The beam cross section and the internal conical shock structure are correlated (Fig. 3.3). Before the first recollimation shock the beam cross section shrinks to an effective radius of $0.7R_b$. After this shock and in the rarefaction the beam reexpands and stretches due to an elliptical surface mode (*e.g.*, Hardee 1996). Between $37R_b \lesssim z \lesssim 50R_b$ the beam flow is influenced by the second recollimation shock, which causes a compression of the beam. A triangular mode seems to grow in this region.

The helical pattern propagates along the jet at a velocity which is intermediate between the jet's head speed and the beam speed[10] which could yield to superluminal components when viewed at appropriate angles. Besides this superluminal pattern, the presence of emitting fluid elements moving at different velocities and orientations could lead to local variations of the apparent superluminal motion within the jet. This is shown in Fig. 3.4, where we have computed the mean (along each line of sight, and for a viewing angle of 40 degrees) local apparent speed. The distribution of apparent motions is inhomogeneous and resembles that of the observed individual features within knots in M87 (Biretta, Zhou, & Owen 1995). In this source, whereas a typical apparent speed of 0.5c is measured for knots A, B and D, small regions within the knots show a large range in speeds (up to 2.5c). Besides that, significant motions transverse to the jet axis were found in knots A, B and C with a trend for

[10] see animation at http://scry.uv.es/aloy.html/JETS/videos/n50p01

larger transverse speeds at larger distances from the nucleus, and specially in the regions where the jet appears to bend and oscillate form side to side.

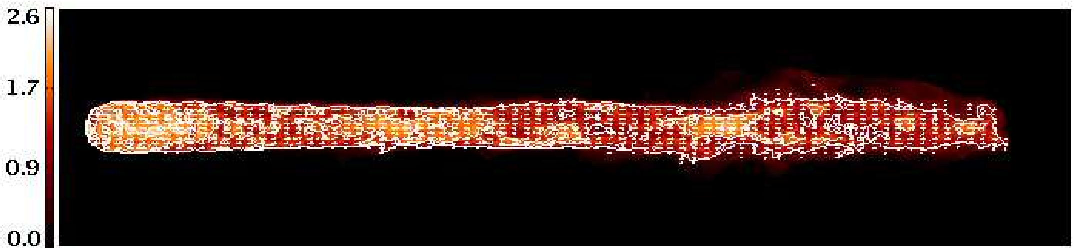

Fig. 3.4.— Mean local apparent speed for the jet of Fig. 3.3 observed at an angle of 40 degrees. Arrows show the projected direction and magnitude of the apparent motion the contours corresponding to values of $1.0\,c$, $1.6\,c$, and $2.2\,c$, respectively. Averages have been computed along each line of sight using the emission coefficient as a weight.

The jet can be traced continuously up to the hot spot which propagates as a strong shock through the ambient medium. Beam material impinges on the hot spot at high Lorentz factors. We could not identify a terminal Mach disk in the flow. We find flow speeds near (and in) the hot spot much larger than those inferred from the one dimensional estimate. This fact was already noticed for 2D models by Komissarov & Falle (1996) and suggested by them as an acceptable explanation for an excess in hot spot beaming.

3.2.3.3. Beam/cocoon shear layer

We find a layer of high specific internal energy (Fig. 3.3d) surrounding the beam like in previous axisymmetric models (Aloy *et al.* 1999a or §3.2.1) although in the specific internal energy is higher in the perturbed models (by more than a factor of 3). A comparison with the backflow velocities (Fig. 3.3e) shows that it is mainly composed of forward moving beam material at a speed smaller than the beam speed. The intermediate speed of the layer material is due to shear in the beam/cocoon interface, which is also responsible for its high specific internal energy. It is possible to characterize the shear layer, in order to have an operative criterion, as the region having a beam mass fraction $0.2 < f < 0.8$.

The existence of such a boundary layer has been invoked as the cause of a smooth deceleration of the material in the jet which offers an admissible explanation for the existence of emission gaps close to the jet basis and the decrease of the jet sidedness ratio with distance from the nucleus (Laing 1996). For appropriate angles to the line of sight, it would be also responsible of the limb brightening of the jets (Komissarov 1990).

De Young (1993) has compared boundary layers in laboratory experiments with the ones in FR Is as inferred from observations to constrain the properties of the ambient medium surrounding these sources. Additionally, De Young has concluded that the very low radio luminosity of the jets in FR IIs and the lack of deceleration may be due to the relatively weak interaction of the jets in these sources with the ambient (*i.e.,* if a boundary layer exists in FR IIs, its relative importance in the dynamics is smaller than in FR Is). However some manifestation of these boundary layers in FR IIs has been reported recently (Swain, Bridle & Baum 1998). Relying on total and polarized radio observations of the jets in the FR II radio galaxy 3C 353 the authors infer that most of the jet emission comes from a thick outer layer where the magnetic field has no component transverse to the jet axis and where the axial and toroidal components are random and approximately in equipartition. The authors suggest as a possible interpretation that the emission layer is a boundary layer where the field is ordered by velocity shear, the apparently lower emissivity near the jet axis being produced by Doppler hidding of emission from fast flowing material in the jet core.

The diffusion of vorticity caused by numerical viscosity is responsible for the formation of the boundary layer. Although being caused by numerical effects (and not by the physical mechanism of turbulent shear) the properties of PPM–based difference schemes are such that they can mimic turbulent flow to a certain degree (Porter & Woodward 1994). Hence, our calculations represent a first approach to study the development of shear layers in relativistic jets and their observable consequences.

The structure of both the shear layer and the beam core are sketched in Fig 3.5. The specific internal energy of the gas in the shear layer is typically more than one order of magnitude larger than that of the gas in the beam core. The shear layer broadens with distance from $0.2R_b$ near the nozzle to $1.1R_b$ near the head of the jet (Fig. 3.6).

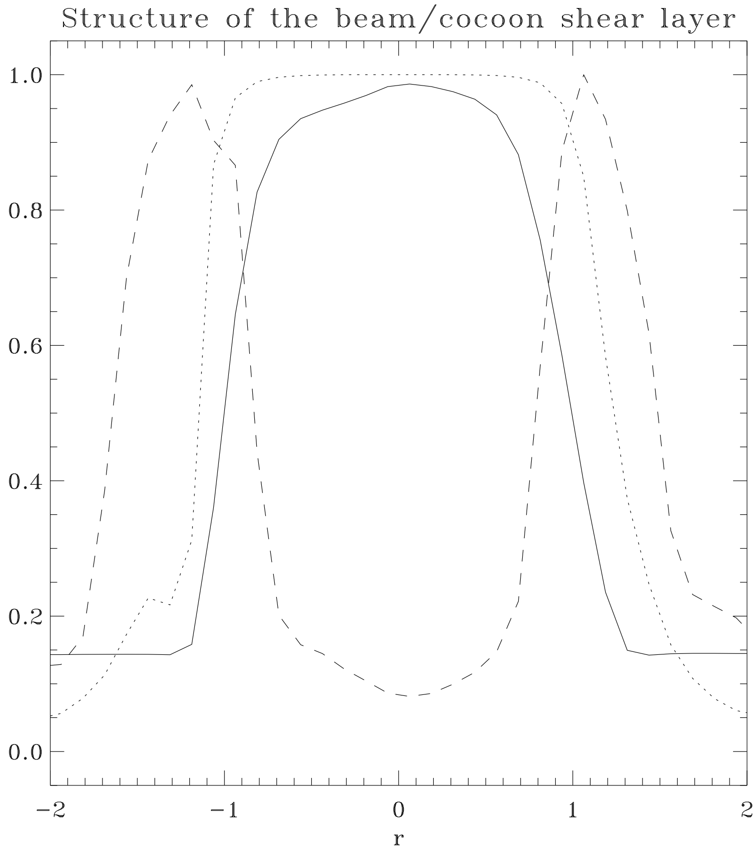

Fig. 3.5.— Beam mass fraction (dotted line), flow Lorentz factor (filled line) and specific internal energy (dashed line), in arbitrary units, accross the beam ($z = 11.7R_b$). Model n50p01.

3.2.3.4. Jet propagation efficiency and disruption

The mean jet advance speed is $0.47c$, but the jet's propagation proceeds in two distinct phases: (i) for $t \lesssim 100$ the jet propagates roughly at the estimated 1D speed ($0.42c$); (ii) for $t \gtrsim 100$ the jet accelerates and propagates faster ($0.55c$). Comparing with the 3D simulation of Norman (1996) we find a similar behaviour: after a short 1D phase and before the deceleration, the jet transiently accelerates to a propagation speed which is $\approx 20\%$ larger than the corresponding 1D estimate. This result contradicts the one obtained by Nishikawa *et al.* (1997, 1998), who found a propagation speed of only 70% of the corresponding 1D estimate in a shorter ($\approx$ 20 normalized time units) simulation of a denser jet. During phase (i) the propagation speed slightly oscillates around the 1D value, a behaviour already found for classical jets (Norman *et al.* 1982) and for axisymmetric relativistic jets (Martí *et al.* 1997). It can be understood in terms of the periodic variations in the terminal shock structure changing from Mach disk to biconical and back. Figure 3.6 shows the axial component of the momentum of the beam particles (integrated across the beam) along the axis, which decreases by 45% within the first $60\,R_b$. Neglecting pressure and viscous effects, and assuming stationarity the axial momentum should be conserved, and hence the beam flow is decelerating. The momentum loss goes along with the growth of the boundary layer whose material is accelerated and heated by viscous stresses. Biconical shocks in the beam are responsible for the break in the axial momentum profiles at $z = 26R_b$ and $z = 50R_b$, because when the beam material passes a conical shock and enters into the adjacent rarefaction fan, it is accelerated by local pressure gradients.

How can the jet accelerate while the beam material is decelerating? Although the beam material decelerates, its terminal Lorentz factor is still large enough to produce a fast jet propagation. On the other hand, in 3D, the beam is prone to strong perturbations which can affect the jet's head structure. In particular, a simple structure like a terminal Mach shock will probably not survive when significant 3D effects develop. It will be substituted by more complex structures in that case, *e.g.*, by a Mach shock which is no longer normal to the beam flow and which wobbles around the instantaneous flow direction. Another possibility is the generation of oblique shocks near the jet head due to off–axis oscillations of the beam. Although difficult to check quantitatively (due to both the lack of an operative definition for Mach disk identification and the present resolution of our simulations[11]) both possibilities will cause a less efficient deceleration of the beam flow at least during some epochs. At longer time scales the growth of 3D perturbations will cause the

[11] In practice, the resolution of our simulations is mainly limited by the available RAM memory of the computer employed

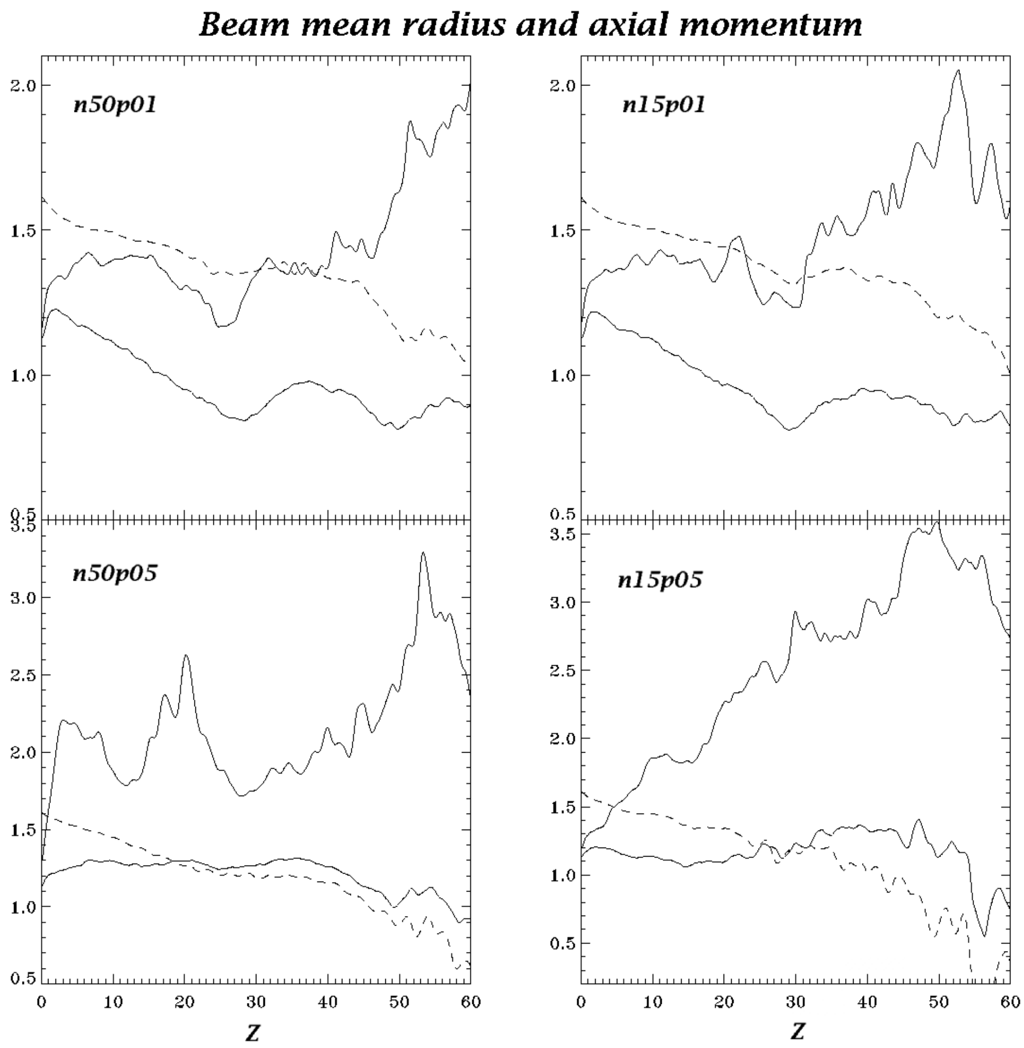

Fig. 3.6.— Into each panel, the dashed line represents the axial component of the momentum of the beam particles (integrated accross the beam) along the jet axis at the end of the simulation. The solid lines mean beam radius as a function of distance for a beam particle fraction $f \geq 0.2$ (top line) and $f \geq 0.8$ (bottom line), respectively. Quantities are in code units.

beam to spread its momentum over a much larger area than that it had initially, which will efficiently reduce the jet advance speed.

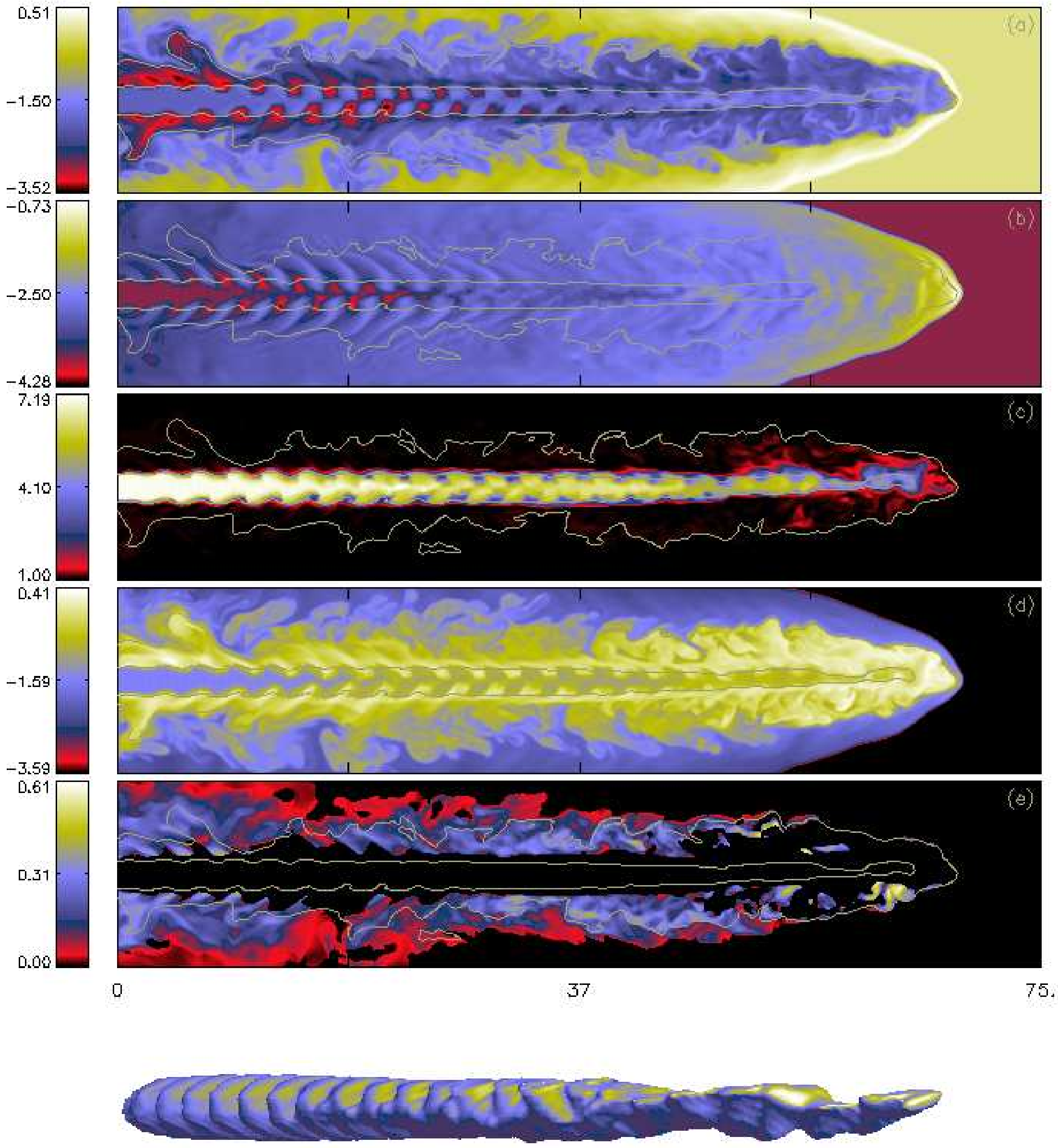

Fig. 3.7.— Same as Fig. 3.3 for model n50p05.

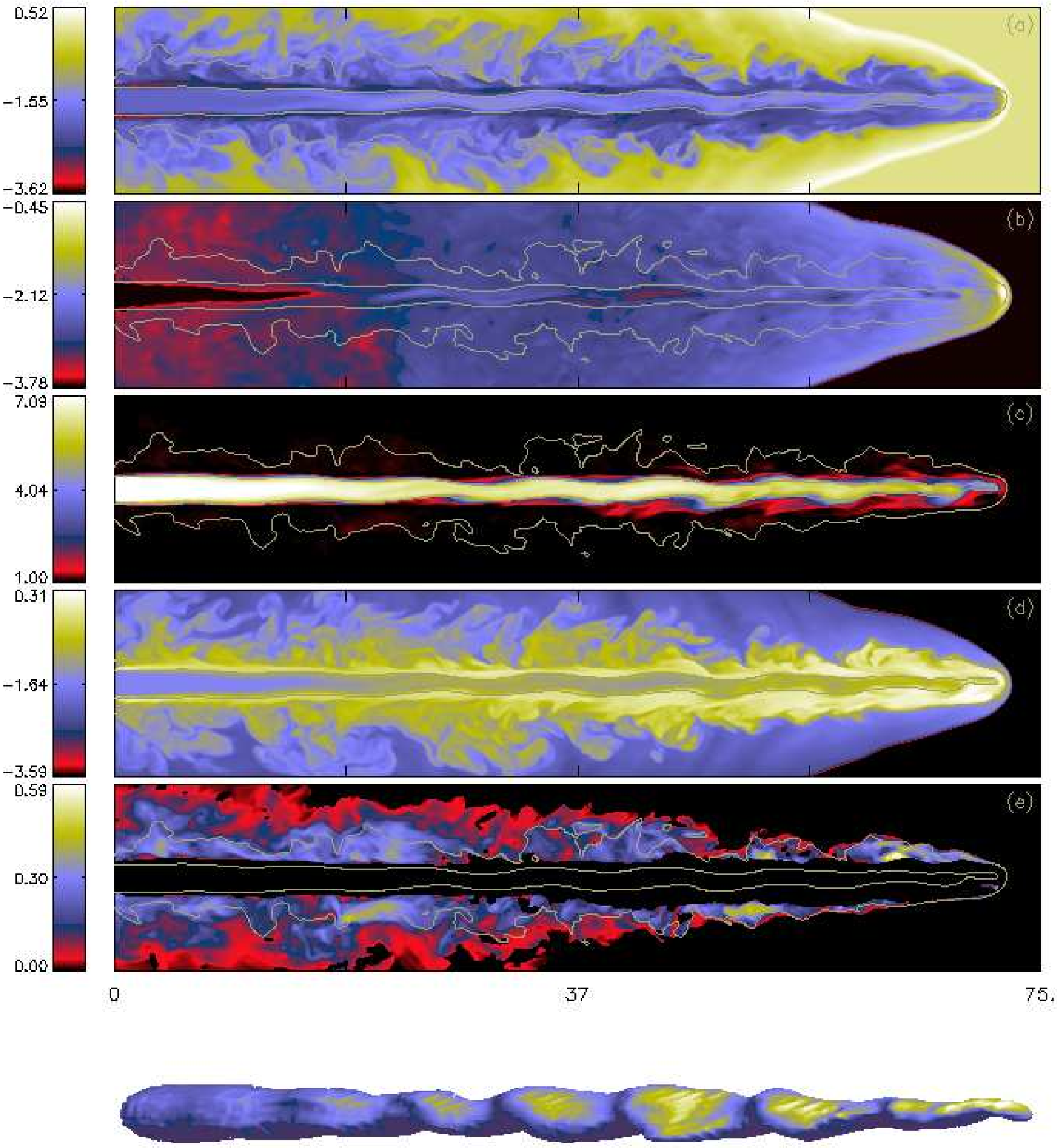

Fig. 3.8.— Same as Fig. 3.3 for model n15p01.

Model	Amplitude (R_b)	λ_p (R_b)	v_h
n15p01	0.2	9.1	0.46
n15p05	1.3	9.0	0.40
n50p01	0.2	3.1	0.48
n50p05	0.4	2.9	0.46

Table 3.2: Approximate numerical values of the perturbation amplitudes, wavelengths and mean jet head propagation speeds of the numerical simulations.

3.2.4. Other models

Next we discuss other models obtained varying the perturbation parameters (Table 3.1). As in the n50p01 case, the evolution of the jets was simulated up to $T \approx 150 R_b/c$. The mean jet propagation speeds (see Table 3.2) lie in the interval $v_h \in [0.4c, 0.5c]$ (compare with $v_{1D} = 0.42c$), so that all of them are still within the 1D phase. Figures 3.7-3.9 show various quantities of the jet in the plane $y = 0$ at the end of the simulation. In every case, the beam structure is dominated by the imposed helical pattern with characteristic wavelengths and amplitudes given in Table 3.2 (to be compared with the values given in Table 3.1 expected from Eq. 3.3).

High frequency modes tend to stabilize the jet despite of the strength of the perturbation, because for $n = 50$, the amplitudes remain below 0.4 R_b, and the morphology is more similar to the non perturbed model (see Fig. 3.2). Low frequency modes seem to be much more perturbed, particularly, the model n15p05 displays the largest off-axis perturbations that, eventually, can made the jet to enter into a disruptive phase on larger time scales. The explanation for this is that for low frequencies of the perturbation, the velocity field at the injection nozzle points into each considered solid angle more time than for high frequencies and, consequently, beam material travels farther in directions normal to the jet axis. Hence, the amplitude of the beam distortion is larger. As expected, the strongest perturbation ($\zeta = 0.05$) induces bigger amplitudes for the same frequency.

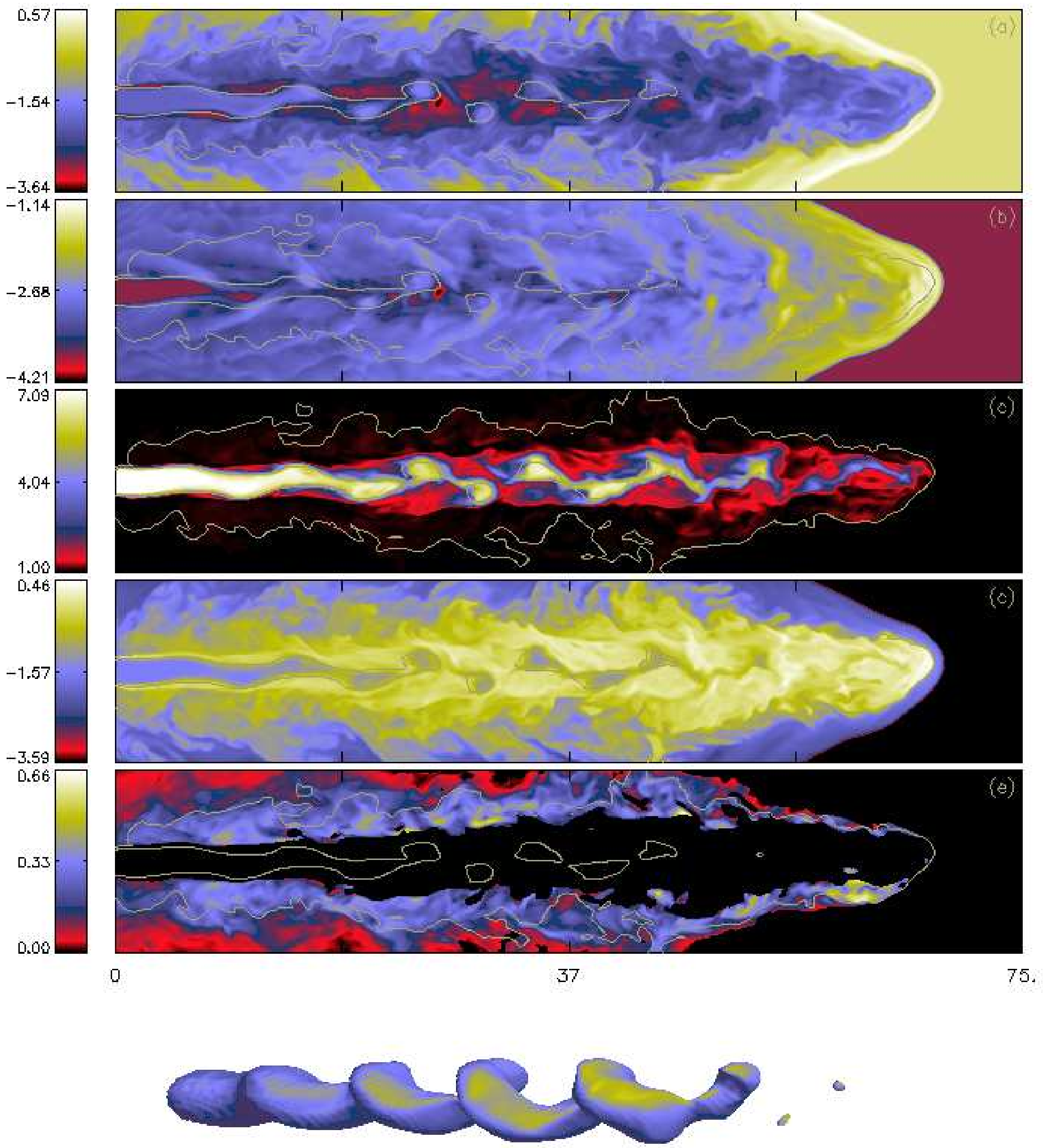

Fig. 3.9.— Same as Fig. 3.3 for model n15p05.

3.2.4.1. Cocoon

Similarly to n50p01, the cocoon is highly turbulent, non-asymmetric and subsonic. It remains quite thin for models with $\zeta_p = 0.01$ but it widens for models with $\zeta_p = 0.05$ ($\sim 3R_b - 5R_b$) as long as the jet propagates efficiently. Nevertheless, the model n15p05 displays a supersonic envelop around the beam formed by material which is dragged by the off-axis perturbed beam material. The beam in this case acts rarefying some regions of a channel (see *e.g.*, the little dark holes at $z = 27R_b$ in panels a and b of figure 3.9) of radius $\sim 1.3R_b$[12]. The dragging effect is due to a mixture of the viscous forces that exist between the beam and the surrounding medium and the Venturi effect that the moving beam material exerts on the surrounding cocooun.

A layer with a relatively high Lorentz factor can be found around the beam (thinner in the models with $\zeta_p = 0.01$ than in those with $\zeta_p = 0.05$), nevertheless, the mean speed of this layer is sub–relativistic ($\sim 0.25c - 0.35c$). The highest backflow velocities ($\sim [0.5c, 0.7c]$) are restricted to a small region in the vicinity of the hot spot (Figs. 3.7-3.9 panels e) and are significantly smaller than in 2D models (consecuently, in no case a relativistic beaming of the counter–jet is feasible). This is due to several factors; the first one is the additional degree of freedom in 3D, which allows the backflow to move in directions different to the one determined by the Z-axis. The second factor is the unrealistically large speeds of the hot spots (see Sect. 3.2.3.4) which prevents fast backflows in models with small perturbations. However, an effect that helps to have larger backflow velocities is the bigger hot spot pressures (see Table 3.3), which favor the acceleration of the deflected beam material, at least for the less perturbed models. For largest perturbation (*e.g.*, model n15p05) the hot spot pressure is smaller than in 2D and, consistently, the propagation speed is the lowest one. Let us remain that $v_h \propto (p_{\rm hs}/\rho_{\rm ext})^{1/2}$, and as can be seen in the second row of Table 3.3 this proportionality is almost confirmed (the constant of proportionality is $\sim 1.42 - 1.93$ for 3D models). Another practical conclusion which may be extracted from Table 3.3 is that the hot spot pressure decreases as the size of the perturbation grows (an explanation for this trend is given below).

[12]This is precisely the perturbation amplitude corresponding to this model.

Model	2D	3D	n15p01	n15p05	n50p01	n50p05
$\log p_{\rm hs}$	-0.82	-0.42	-0.45	-1.14	-0.51	-0.73
$\frac{\sqrt{p_{\rm hs}}}{v_h}$	1.79	1.93	1.74	1.42	1.61	1.51

Table 3.3: Values of the hot spot pressure for the unperturbed (2D model C2 of Martí *et al.* 1997, and 3D axisymmetric reference model) and perturbed models at the end of each simulation. The second row shows the constant of proportionality between the hot spot pressure and the mean velocity of the head.

3.2.4.2. Beam and Hot spot

The models with low frequency or high ζ_p value display some twisting, flattening and local deflections of the jet head, although no evident signs of filamentation have been found (see beam mass fraction isosurfaces on Figs. 3.3, 3.7 – 3.9). However, it is remarkable that nor these 3D effects is strong enough to break the beam neither they grow significantly over the linear regime to be disruptive during the simulation run time. Even if this may be a sign of stability, let us remind the reader that in Sect. 3.2.2 we argued that our simulations were still in the 1D phase and, furthermore, our simulations have run for a "physical time" two orders of magnitude smaller that the real sources, and therefore, the perturbations might not have had enough time to grow substantially.

Within the beam the perturbation pattern is superimposed to the shocks. To determinate the location of the shocks we have considered the relative increments of the averaged pressure over each cross section of the beam ($\bar{p}^b_k$[13]). The results are plotted on Fig. 3.10, where the most significative feature is the relative maximum of $\bar{p}^b_k$ in the interval [26, 29] R_b. This fact, together with the increment in density and the jump in velocity, allows us to conclude that the maximum is associated to a recollimation shock. In the 2D axisymmetric case, considering that the evolution

[13]The mathematical definition of this variable is: $\bar{p}^b_k = \frac{\sum_{i,j,f_{ijk}>0.85} p_{ijk} f_{ijk} \Delta x_i \Delta y_j}{\sum_{i,j,f_{ijk}>0.85} f_{ijk} \Delta x_i \Delta y_j}$

of the model C2 has arrived only to 130.23 R_b/c, the first recollimation shock is at 17 R_b(the second shock $\sim 34\,R_b$). The recollimation effect is seen in isosurfaces of f (Figs. 3.3, 3.7 – 3.9) and is presented in Fig. 3.10 as a decrement of $\bar{p}_k^b$ which is inversely proportional to the beam cross section.

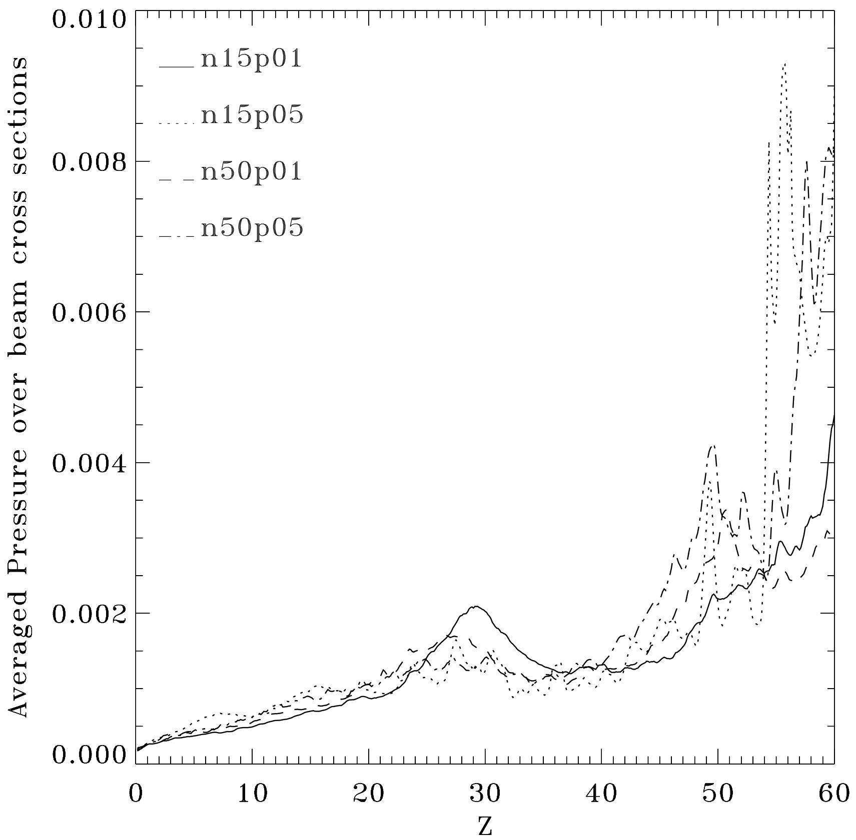

Fig. 3.10.— Averaged beam pressure over each beam cross section.

In the less perturbed models, another recollimation shock is seen at about 50 R_b. This shock seems to disappear in the model n15p05. An acceptable explanation is that all the models are produced as perturbations on a reference axisymmetric one which has the first biconical shock at about 27 R_b, so that it is natural that the structure of the reference model is partially retained by the perturbed ones at least during an initial phase. This justifies the presence and location of the first shock (it is closer to the injection point and the estructure within this region is still dominated by the initial data). However, as the jets evolve the non linearity of the modes excited by the perturbation give rise to a quantitatively different morphology at larger scales. A confirmation of this point is that the beam in the model n15p05 is highly distorted after $50\,R_b$, and the main shock structure is almost lost.

The beam structure is very similar for the models n50p01 (Fig. 3.11) and n15p01 (Fig. 3.13) and, in both cases an effective radius of $0.7R_b$ results from the stretching of the beam cross section (see subsection 3.2.3.2) between the first and the second recollimation shock. Of course, the main difference between both models is that the amplitude of the perturbation is larger for n15p01 than for n50p01 and, consequently, the *beam local axis* oscillates more in n15p01 than in n50p01.

The models n50p05 (Fig. 3.12) and n15p05 (Fig. 3.14) show a smaller contraction of the beam after the first recollimation shock. In the model n50p05, the perturbation symmetrizes the beam shape in such a way that it seems almost circular up to $\sim 33\,R_b$. Then, the cross section shrinks and starts to develop a triangular mode at $\sim 48\,R_b$. Approximately $10\,R_b$ farther this mode is about to break in filaments the beam. The model n15p05 is actually so perturbed that is difficult to evaluate the effect of the shock on the beam structure. Additionally, due to the large off-axis oscillations the shape of the beam is highly distorted by elliptical modes (starting at $\sim 24\,R_b$), triangular modes (at $\sim 37\,R_b$) and other non linear effects. Let us remark that is possible that filaments on the beam are not seen due to the numerical diffusion inherent to the advection of the beam mass fraction.

The helical pattern propagates along the jet at different velocities, depending on the perturbation. While for models less perturbed it is closer to the beam speed, for the more perturbed ones it is nearly equal to the head's velocity (*e.g.,* in n15p01 and n15p05 this velocity is ~ 0.46, while their head's velocities are 0.46 and 0.40 respectively). Given that the presence of emitting fluid elements moving at relativistic speeds in non axial directions can lead to local superluminal motions for favored angles to the line of sight, we have analyzed these possibilities: (i) apparent speeds much larger than the one expected for a Lorentz factor ≈ 7 at a certain viewing angle, (ii) large apparent transverse motions in our models by computing the mean (along each line of sight and for a viewing angle of 40 degrees) local apparent speed of all the fluid elements as if they were emitting flows (Fig. 3.4 with arrows showing the magnitude and projected direction of the apparent motion), and (iii) inhomogeneous distribution of apparent speeds. We find that for model n50p01, the first possibility

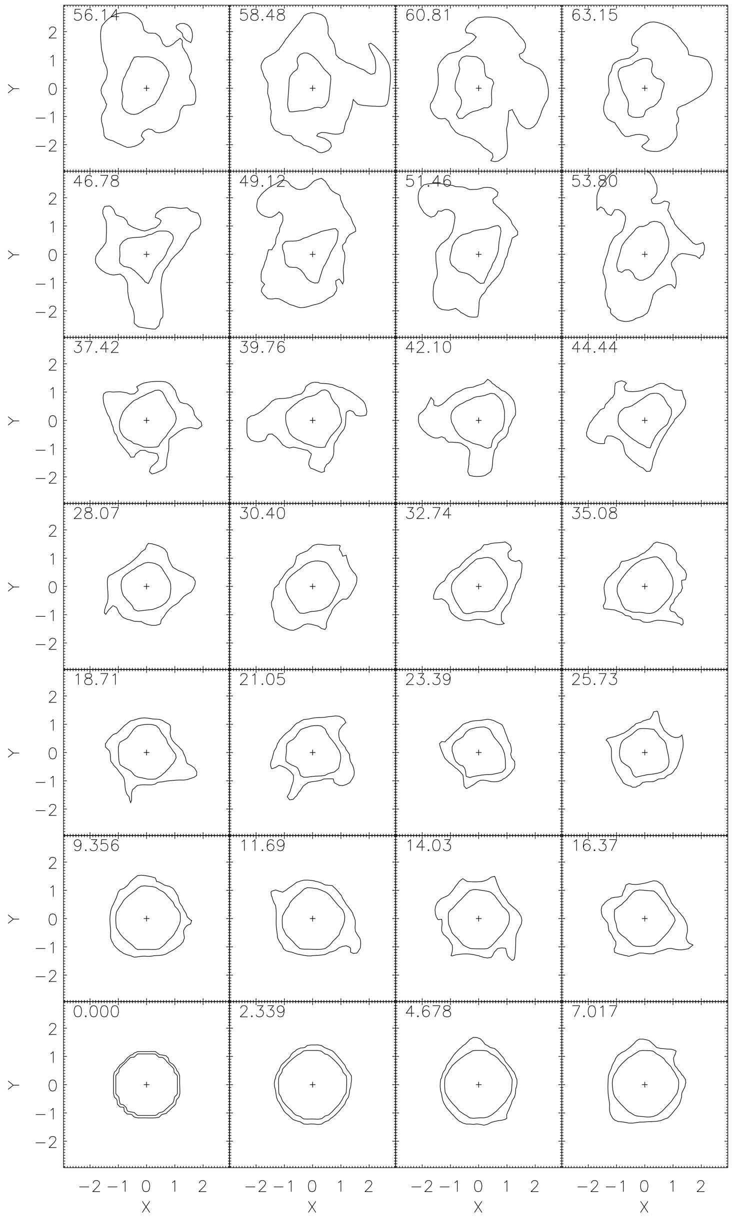

Fig. 3.11.— Shape of the beam mass fraction levels 0.2 and 0.8 for model n50p01 at different distances from the injection point. The central cross represents the $z-$axis.

is rejected because, for the considered viewing angle, the maximum apparent velocity computed is ~ 2.63, which corresponds exactly with the theoretical maximum for the beam speed at the injection point. The second possibility is not completely discarded, although the range of apparent velocities lies in the expected (theoretical)

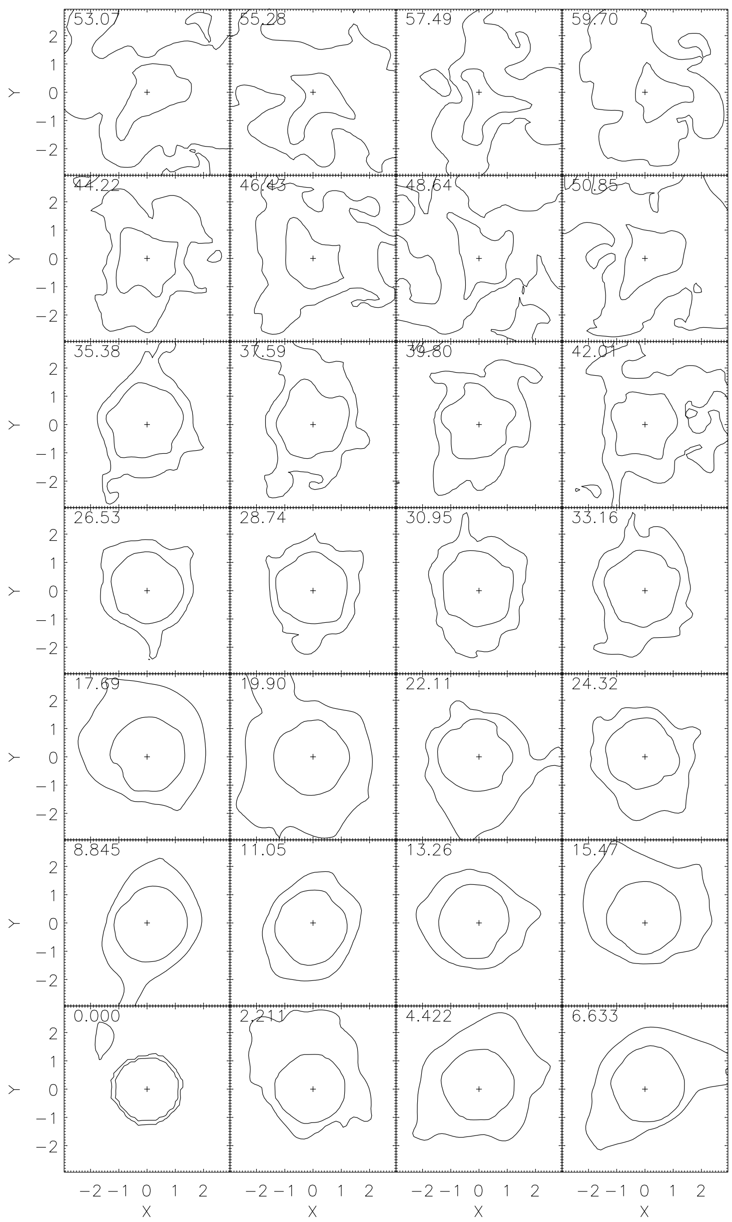

Fig. 3.12.— Same as Fig. 3.11 for model n50p05.

range. However, it is true that we can see a distribution of apparent velocities which is not axisymmetric, and it is the result of the fact that, at the considered time, a number of fluid elements have velocities pointing towards the observer (and this points are enhanced) while other may point in any other direction (having a smaller

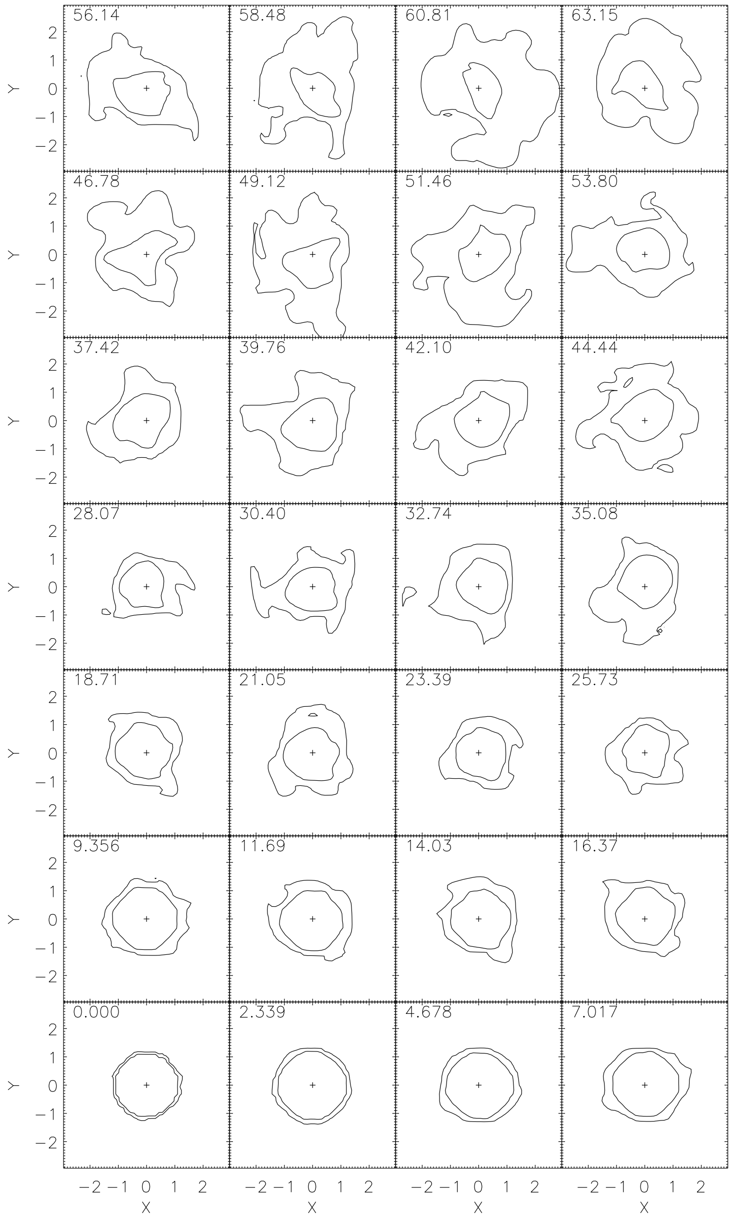

Fig. 3.13.— Same as Fig. 3.11 for model n15p01.

Doppler boosting). Variations of this kind in the apparent velocity field have been found in *e.g.*, M87 (Biretta, Zhou & Owen 1995). The analysis of other models is still not done, however, we expect that all of them satisfy the third possibility. We believe that the model n15p05 is a good candidate to fulfill the second possibility

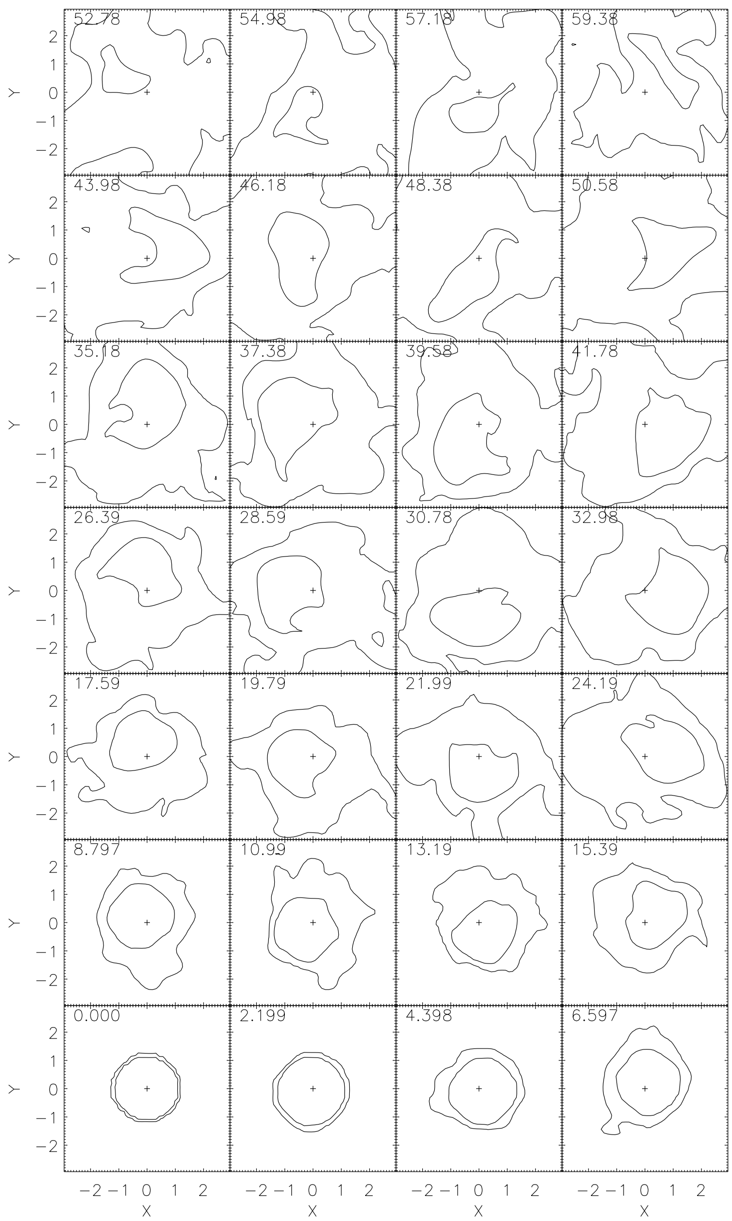

Fig. 3.14.— Same as Fig. 3.11 for model n15p05.

because it displays the largest out of axis motions. In addition, for some angles to the line of sight close to the pitch angle of the helical pattern (roughly 40°; Fig 3.9c) a set of separate components moving with the velocity of the pattern are feasible (although a more detailed analysis is necessary in order to be sure of this assertion).

3.2.4.3. Beam/cocoon shear layer

The layer of high specific internal energy (Figs. 3.3, 3.7 – 3.9 panels d) surrounding the beam and moving forward at a velocity smaller than the beam speed (Figs. 3.3, 3.7 – 3.9 panels e) is present in all the models, but it is more distorted in the more perturbed ones.

The structure of both the shear layer and the beam core are sketched in Figs. 3.5, 3.15 – 3.17 (these figures show one dimensional cuts at a distance of $z = 11.7\,R_b$ from the origin). The specific internal energy of the gas in the shear layer is, in every model, typically more than one order of magnitude larger than that of the gas in the beam core. Table 3.4 shows the approximate range of variation of the width of

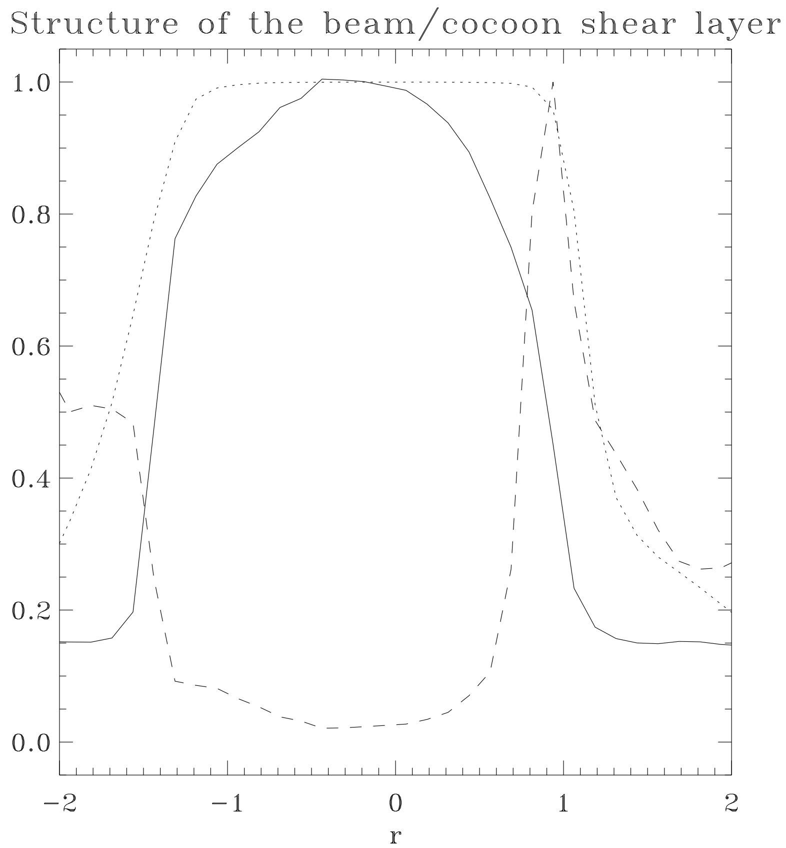

Fig. 3.15.— Same as Fig. 3.5 for the model n50p05.

the core and the shear layer for the models analyzed here. The shear layer broadens with distance from $\sim 0.2\,R_b$ near the nozzle to a value near the head of the jet which is different for every model. Nevertheless, the maximum width of the layer grows with the perturbation size and decreases with the frequency. This trend is shown in Fig. 3.6, where the solid lines display the mean radius as a function of the axial position for the two values of f that determinate the limits of the shear layer.

Model	r_c	Δr_s
n50p01	1.1-0.8	0.2-1.1
n50p05	1.1-0.9	0.2-1.6
n15p01	1.1-0.7	0.2-1.1
n15p05	1.1-0.7	0.2-2.0

Table 3.4: Width of the beam core and shear layer. Values at the left of the variation intervals correspond to values near the injection position whereas values at the right correspond to values near the jet head.

One can realize that the inner part of the shear layer (lower solid lines in the figure) behaves differently for different values of ζ_p. For the models n50p01 and n15p01 the layer grows inwards up to the first recollimation shock ($\sim 26\,R_b$) then it expands and shrinks again reaching a new local minimum at the second recollimation shock ($\sim 48\,R_b$). However, for $\zeta_p = 0.05$ the inner boundary of the shear layer is almost uniform up to $\sim 40\,R_b$ and then it decreases in radius (faster in model n15p05).

A more detailed picture of the shape of the cross section of the shear layer is given by the isocontours $f = 0.2$, 0.8 in Figs. 3.11 – 3.14. Evident signs of disruption of the layer are located from $44\,R_b$ and after, particularly in model n15p05, in which the fixed width selected to display the shear layer (a $3R_b \times 3R_b$ window centered on the initial axis of the simulation) is not enough to capture the full extension of the layer.

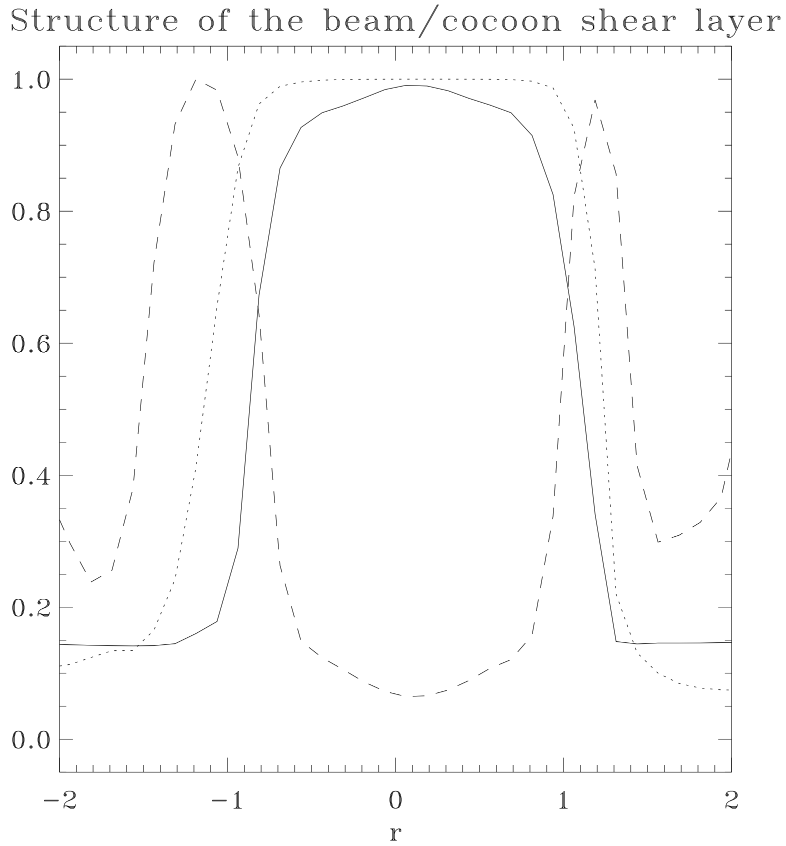

Fig. 3.16.— Same as Fig. 3.5 form the model n15p01.

3.2.4.4. Jet advance and disruption

The evolution of the head's position for every model is displayed in Fig. 3.18. It is noticeable from the head's position at the end of the simulation that the mean jet advance speeds are unrealistically large (the exact values are written in Table 3.2), even larger than the 1D estimated speed of $0.42c$ (except for model n15p05). All the models propagate following two distinct phases which are delimited by a *turning time* (t_{12}) lying in the interval $[85, 110]$, when the head of the jet has propagated along $40\,R_b$. These phases are characterized by different propagation speeds, v_1 (phase 1) and v_2 (phase 2) that are presented in Table 3.5. The general behavior is that the jet starts to propagate with a velocity of $0.43c - 0.45c$, which is close to v_{1D} (but a bit larger). Then, most of the models accelerate at considerably larger speeds (about 9% to 26% larger than the previous v_1 velocities). Contrary to this general

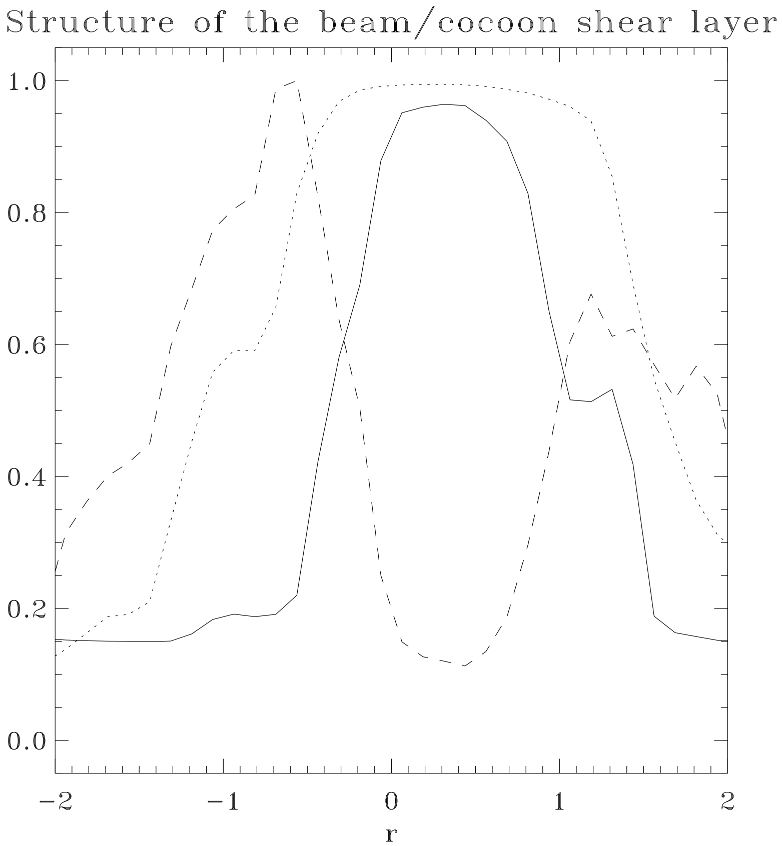

Fig. 3.17.— Same as Fig. 3.5 form the model n15p05.

trend, the model n15p05 decelerates up to $v_2 = 0.37c$. This is again a result of the applied perturbation because as mentioned in previous sections, the cross section of the beam at the jet end is bigger than in the rest of the models. Consequently, the effective advance surface is larger too, and, in addition, the hot spot pressure is the lowest one (see Table 3.3), allowing for a smaller head speed.

From Fig. 3.6 we infer the same qualitative conclusion for all the models than for n50p01 (see 3.2.3.4). The axial component of the momentum of the beam particles decreases and hence the beam flow is decelerating. However, the degree of deceleration is very different for models with $\zeta_p = 0.05$ (the axial momentum at $60\,R_b$ is a factor $\sim 2.7 - 4$ smaller than at injection nozzle) than for those with $\zeta_p = 0.01$ (an smooth momentum loss of $\sim 50\%$ is noticeable in the first $60\,R_b$). This behavior is

Model	v_1	v_2	t_{12}	z_{12}
n50p01	$0.43c$	$0.54c$	85	36
n50p05	$0.45c$	$0.49c$	93	42
n15p01	$0.43c$	$0.52c$	110	46
n15p05	$0.44c$	$0.37c$	80	35

Table 3.5: Velocities of the heads of the jets in each propagation phase. t_{12} and z_{12} are the times and distances that separate the two phases (both quantities in code units).

explained in terms of the growth of the boundary layer (see 3.2.3.4), since this layer is bigger (so that the dissipation of axial momentum due to viscous stresses –which depend on the extension of the contact surface– is bigger) for the strongest perturbation (Figs. 3.12, 3.14) than for the smallest one (Figs. 3.11, 3.13). Furthermore, the strength of the perturbation by itself motivates a change of axial into non-axial momentum, because for $\zeta_p = 0.05$ we are putting in non-axial directions five times more momentum than in the case $\zeta_p = 0.01$. Actually, the perturbation drives the beam along a twisted path instead of along a right one (as in the axisymmetric case), and in order to twist the path, a part of the initial axial momentum is needed. The momentum loss rate is almost constant into the first $40\,R_b$ (of course, it is steeper for $\zeta_p = 0.05$), and then enters into an oscillatory phase which coincides with a region where the cocoon is particularly turbulent and perhaps large external mass entrainment is taking place.

Even if the beam material is decelerating most of the models (except n15p05) accelerate after t_{12}. The suggested mechanism to account for this acceleration has been proposed in subsection 3.2.3.4. However, we expect that at longer time scales the growth of the perturbations will spread the momentum of the beam over a much larger area than that it had initially, reducing the jet advance speed (actually, this is the mechanism that we has started to work for n15p05 –the model having the largest cross sectional area near the head of the jet–).

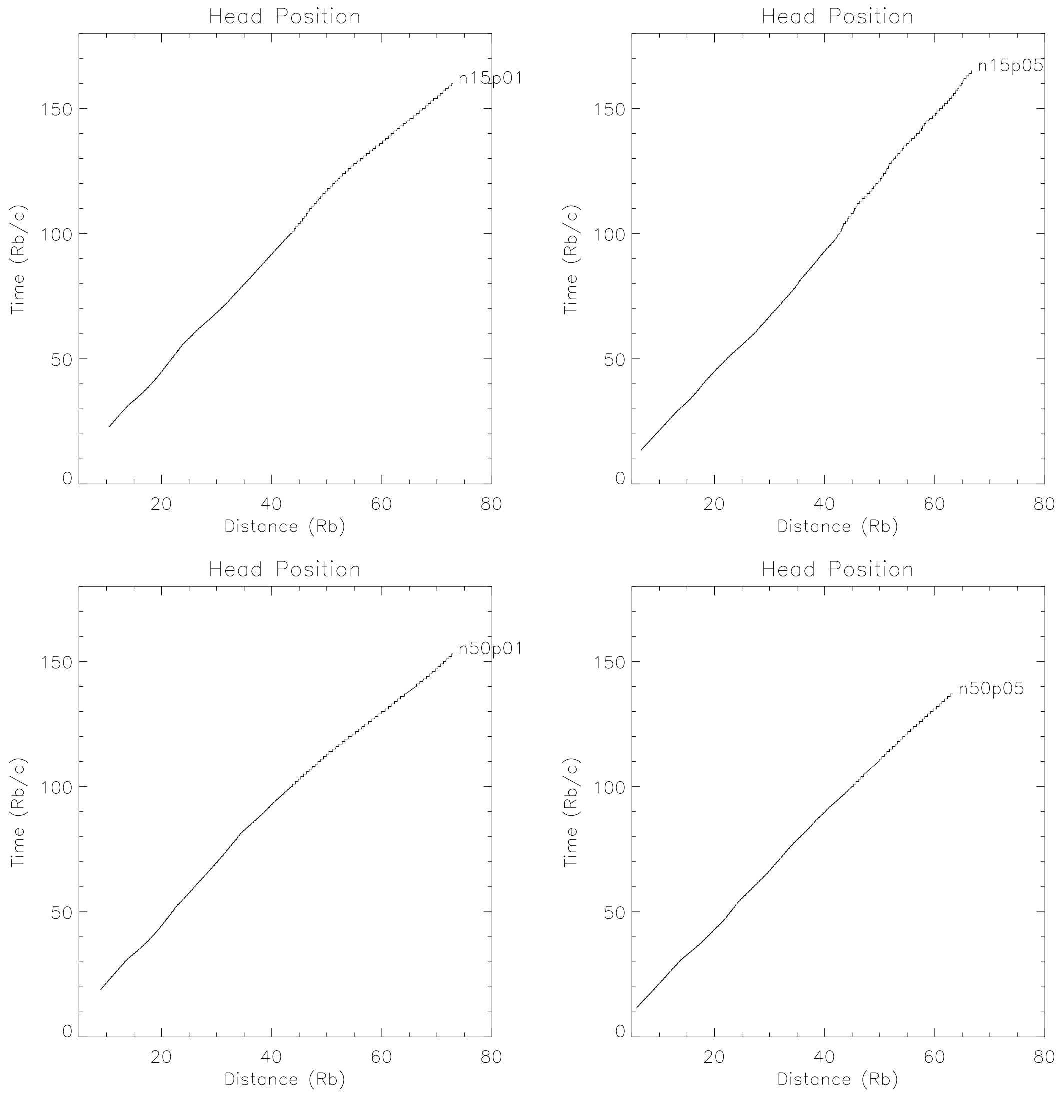

Fig. 3.18.— Evolution of the head's position for every numerical model.

3.3. Emission from 3D relativistic jets

Since the radio-emission is the observable signature of the astrophysical jets, we need to be able to produce radio maps in order to explain totally or partially (*i.e.,* some features) the existent observations. VLBI imaging of some radio-loud AGNs revealed the presence of narrow cones or jets where the radio emission was mainly concentrated, and another smaller regions or components where the emission was more powerful. These components may move at apparent superluminal speeds which is explained in the framework of the standard model (see *e.g.*, Pearson *et al.* 1981, or Sect. 3.1.2) considering a relativistic jet ($W \sim 10$) viewed at small angles to the line of sight.

The analytical models aiming to explain the appearance of radio jets were developed by Jones & O'Dell (1977a,b), Marscher (1980), Marscher & Gear (1985) and Königl (1981). They studied the spectrum of the synchrotron emission produced in different parts of the jet and the perturbations induced on the spectrum of such emission due to the jet inhomogeneities. The inhomogeneities were introduced to mimic the ejection of components in real sources. Such ejections are usually preceded by outbursts in emission at radio wavelengths, whose frequency dependent light curves of both total and polarized flux were successfully interpreted as traveling shock waves (over the underlying steady jet). The three regions in which the jet was divided came from BR74 and, of course, this division relies on a simplified hydrodynamical model (actually, the jet shape is theoretically inferred instead of being the result of a complete numerical calculation).

The standard emission model assumes that the jet (at pc scale) is inertially confined, and it is characterized by its Lorentz factor, the half-opening angle and the distance to a given starting point (the fiducial point). The jet is formed by an ultrarelativistic plasma described as an ideal gas EOS with constant adiabatic index ($\gamma = 4/3$). The plasma is magnetized and the charged particles (electrons, ions or positrons) follow helicoidal paths around the magnetic field lines. Given that the particles are accelerated (due to the helicoidal trajectory), they will emit electromagnetic radiation (the synchrotron radiation). The variations of the magnetic field, the number density per unit of energy, etc., are determined by the adiabatic expansion of the jet. The presence of shocks in the fluid is allowed and they are supposed to comprise two fronts (forward and rear fronts; see Hughes *et al.* 1985) in order to connect the shocked region with the steady jet.

The detected synchrotron emission in the ultraviolet, optic and infrared bands comes from the innermost parts of the jet, which are optically thick to the radioemission. The maximum in the radio band is produced where the Lorentz factor, and hence the Doppler boosting, is maximum. This region is usually identified as the radio-core. The rest of the external part of the jet is optically thin at radio frequencies.

The radiation density in the innermost parts of the jet is a bit larger than the energy density associated to the magnetic field. This makes possible that the relativistic electrons interact with the photons coming from the synchrotron emission increasing their energy (of the photons). This process is known as *synchrotron-self Compton* (SSC). Using this mechanism either X-rays (by first order scattering) or gamma-rays (by second order scattering, being more energetics because the photons have interacted twice with the electrons) are produced. In this region, the internal energy of the relativistic plasma is converted into bulk kinetic energy and the jet accelerates (Marscher 1980; Maraschi *et al.* 1992).

The external part of the jet is characterized by the synchrotron emission in radio and is observed using VLBI. Here the jet does not accelerate any more and expands adiabatically. The conservation of the magnetic flux along with the adiabatic expansion produce a decrease of the magnetic field and the particle density along the jet and, consequently, the synchrotron emission.

The theoretical models gave rise to more detailed numerical models (*e.g.,* Jones 1988; Hughes, Aller & Aller 1989a, b; Marscher, Gear & Travis 1992; Gómez, Alberdi & Marcaide 1993, 1994; Gómez *et al.* 1994) trying to validate the underlying theory and to get the physical jet parameters which were able to match the observations of some sources. However, all these previous works (as the theoretical models) were limited by an oversimplified hydrodynamical evolution (result of the solution of the one-dimensional RHD equations). Such restriction has motivated the combination of RHD in 2D with the calculation of the synchrotron radiation transfer at pc scales. The first numerical simulations of the pc scale synchrotron emission from hydrodynamic relativistic jets were presented in Gómez *et al.* (1995). Since then, other works have followed this idea (Gómez *et al.* 1997; Duncan, Hughes & Opperman 1996; Mioduszewski, Hughes & Duncan 1997; Komissarov & Falle 1997). From their simulations these authors inferred that the observations of such sources can be explained in terms of traveling perturbations (or shocks) in steady relativistic jets. Other important consequence of this description has been the establishment of the rôle played by the external medium in determining the jet opening angle and the presence and positions of standing shocks (actually, the opening angle is a consequence of the external medium pressure gradient).

The present work follows the same algorithm to evaluate the emission from 3D relativistic jets than in Gómez *et al.* (1995). The key points of this method are two: (1) the jet structure is calculated using a relativistic time-dependent hydrodynamical code and (2), the radio emission from the model jets is calculated by integrating the transfer equations of synchrotron radiation, accounting for the appropriate opacity and relativistic effects, such as Doppler boosting and relativistic aberration. The first part is made here by using GENESIS, and we have employed the same hydro-simulations than in the previous sections. The radio emission, has been calculated with the same code than in Gómez *et al.* (1994, 1995 and 1997) and, for the sake of completeness, we explain in the Appendix D the basic ingredients of the calculations involved in what the emission concerns.

Gómez *et al.* (1995) approach relies on several physical hypothesis like, *e.g.*, that the particle and energy density of these non-thermal electrons at the jet inlet are assumed to be proportional to the thermal electrons, which dynamics are computed using our relativistic hydrodynamical simulations, *i.e.*, emissivity of the jet is computed from the high energy relativistic non-thermal electrons. This approach has been followed previously by different authors (Rayburn 1977; Wilson & Scheuer 1983; Mioduszewski, Hughes, & Duncan 1997; Komissarov & Falle 1997) as well as by Jones, Tregillis & Ryu (1999), as the initial assumption before allowing radiative loses or accelerations by shocks to change the energy distribution of the non-thermal electrons.[14] It is therefore a common basic *ansatz* when studying the emission of jets in AGNs using hydrodynamical simulations.

The validity of our assumption can be asserted by considering that the total energy carried by the non-thermal electrons is significantly smaller than for thermal gas, and therefore they are expected to share the same dynamics than the simulated relativistic thermal gas. Any exchange between internal and kinetic energy

[14] In such work, the non-thermal flow is assumed to share the dynamics of their non-relativistic computed flow.

along the jet will maintain the proportionality between thermal and non-thermal electrons. Only gains by particle acceleration in shocks or losses by radiation can modify this proportionality. In the model presented in this memory we are only interested in studying the emission at radio wavelengths, for which the loses can be neglected (specially taking into account that in our model the magnetic field to thermal particle energy ratio is small –see below–). We are only interested in studying the emission from the jet, neglecting the hot spot and the cocoon, where no strong shocks are found (see also Jones, Tregillis & Ryu 1999). Therefore, we do not expect to have strong particle accelerations that could influence the non-thermal spectra, and hence our emission calculations. Furthermore, the emission distribution is not influenced by the particular value chosen for the proportionality between the non-thermal and thermal electrons. It would only change the final quantitative emission values, something that is unimportant in our results.

The magnetic field energy is set to be locally proportional and significantly smaller than the particle energy density. Therefore, although the structure of the magnetic field is set in a certainly arbitrary way, we can be confident that the jet dynamics will not be influenced by the field. Non relativistic MHD simulations of Jones, Tregillis & Ryu (1999) show that even with "weak" magnetic fields there are numerous places in the cocoon where magnetic, Maxwell stresses are significant. Is therefore in the cocoon where the strongest shocks and magnetic influence in the jet dynamics are found, not in the jet itself. We explicitly neglect the emission from the cocoon and hot spot, consistently, our approximation of considering the jet dynamics unaffected by the magnetic field (as well as neglecting the radiative losses in the emission at radio wavelengths) seems completely appropriated. Once the magnetic field has been chosen dynamically unimportant, we are allowed to consider different, certainly *ad hoc*, magnetic field jet geometries.

In this memory we study for the first time the radio emission properties of three-dimensional relativistic hydrodynamical models, focusing on the observational consequences of the interaction between the relativistic jet and the surrounding medium, leading to the development of a shear layer[15]. The presence of such a

[15] The following sections gather and develop the work done in Aloy *et al.* (1999c).

shear layer (with distinct kinematical properties and magnetic field configuration) has been invoked *ad hoc* in the past by several authors (Komissarov 1990, Laing 1996) to account for a number of observational characteristics in FR I radio sources but, its physical nature is still largely unknown. Recently, Swain, Bridle, & Baum (1998) have found evidence of such shear layers in FR II radio galaxies (3C353), and Attridge, Roberts, & Wardle (1999) (ARW99, henceforth) have inferred a two-component structure in the parsec scale jet of the source 1055+018.

3.3.1. Jet Stratification: Beam and Shear Layer

The hydrodynamical model we have used to study the emission properties of relativistic jets is n50p01. The model is characterized by a two-component structure (see Fig. 3.19) with a fast ($W \sim 7$) inner jet and a slower ($W \sim 1.7$) shear layer with high specific internal energy. We define for practical purposes the shear layer as the region with the beam particle fraction between 0.2 and 0.95[16], represented with white contours in Fig. 3.19 (0.95 for the inner contour). Although, as discussed in Sect, 3.2.3.3 the numerical viscosity inherent to our code is the responsible for the formation of the shear layer and not the turbulent shear, it allows us to obtain the first approach to study the physics of shear layers in relativistic jets and their observational consequences. The width of the shear layer, Δr_l, increases with the distance from the nozzle from a value $\Delta r_l \sim 0.2$ near $z = 0$ to $\Delta r_l \sim 0.65 - 1.0$ at $z = 68 R_b$. The broadening of the shear layer is due to the transfer of momentum of the inner jet. As shown in Fig. 3.6, the axial component of the momentum of the beam particles decreases by a 30% within the first 60 R_b. The transfer of momentum conveys a decrease in the Lorentz factor in the inner jet with values $\sim$ 5.8, 5.3, and 4.8 at $z =$ 25, 50, and 68 R_b, respectively.

The computed hydrodynamical structure of the jet agrees with the proposed in two-component jet models (Komissarov 1990, Laing 1996), also revealing a high energy in the shear layer not considered in previous theoretical models. This rela-

[16]Note that in Sect. 3.2.3.3 we defined the *hydrodynamical* shear layer as the fluid having $0.2 < f < 0.8$. Here we have extended inwards (to the axis o the jet) the upper limit of the shear layer because it fits better with some observations (see below).

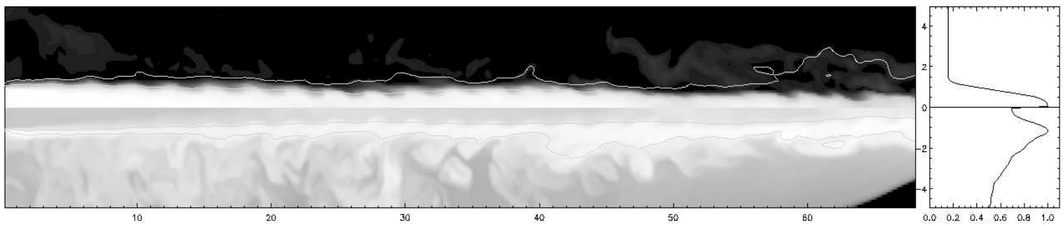

Fig. 3.19.— Cuts of the Lorentz factor (top half panel) and specific internal energy (bottom half panel) distributions of the hydrodynamical model along the plane $y = 0$. White contours representing constant values of the beam particle fraction (0.95 for the inner contours, 0.2 for the outer ones) are used to characterize the shear layer. Rightmost plots show the average, along lines x =constant, of the corresponding distributions across the jet.

tively higher internal energy in the shear layer has specific observational evidence, as shown in the following sections.

3.3.2. Emission properties

In order to study the emission properties of large scale jets in AGN, we need to establish the actual structure of the magnetic field within the jet. For this, the magnetic energy is set to be locally proportional and significantly smaller than the particle energy density, hence being dynamically unimportant. Different *ad hoc* distributions of the magnetic field in the jet spine and shear layer can be considered, allowing us to test different models for the observed jet polarization stratification. In our model we assume that the jet magnetic field compress two components: a toroidal field present in both, the jet spine and shear layer, and a second component (in equipartition with the toroidal field) aligned in the shear layer, and radial in the jet spine. The aligned component in the shear layer may be the result of shear between the jet and external medium, while the radial field in the jet spine can arise from transverse shocks (i.e., ARW99). The resulting magnetic field will be aligned in the shear layer, and perpendicular in the jet spine, as suggested by several observations (Laing 1996; Swain, Bridle, & Baum 1998; ARW99). In order to reproduce the observed relatively low degrees of polarization, an extra randomly oriented magnetic field component is assumed for the shear layer and jet spine. The random field is considered to contain 60% of the total magnetic field energy, obtaining degrees of polarization below $\sim 40\%$. The Stokes parameters that determine the emission are calculated following the prescriptions given in Ap. D.

Since only jet material is expected to radiate, we have multiplied the proper rest–mass density by the beam particle fraction. We are only interested in studying the emission properties of the stratified jet (beam and shear layer), hence we neglect the relatively small emission that can arise from the jet cocoon by limiting the calculations to values of the beam particle fraction above $f = 0.2$. We also ignore the emission from the hot spot, which due to its relatively young evolved state would out shine the rest of the jet. For this, we limit the calculations to the inner $68R_b$.

3.3.2.1. Total and polarized emission stratification as a function of the viewing angle

Because of the highly relativistic speeds in the jet, the emission is mainly determined by the observing viewing angle, Θ, through the Doppler factor and light aberration. The different velocities and magnetic field configurations in the beam and shear layer would then result in substantially different total and polarized emission structure as a function of the viewing angle.

Figures 3.20 and 3.21 show the computed emission from the hydrodynamical model n50p01, corresponding to a viewing angle of 50° and 10°, respectively. The emission is computed for an optically thin observing frequency, an spectral index of the electrons of 2.4. For relatively large viewing angle, as in Fig. 3.20, the jet emission is limb brightened. This is in part due to the higher specific internal energy in the shear layer, resulting in a larger synchrotron emission coefficient. On the other hand, the rôle played by the Doppler factor (see Eq. D13) can either enhance or cancel the limb brightening, as a function of Θ. For $\Theta > 1/W$, the emission is dimmed, while for $\Theta < 1/W$ the emission is boosted in the observer's frame. Because of the jet velocity stratification (see Fig. 3.19), for $\Theta > 1/W$ the fast jet spine suffers a larger amount of dimming than the shear layer, enhancing the limb brightening. For the jet model we study, with a mean $W \sim 7$ in the jet spine, this is maximized for $\theta \sim 50^\circ$, for which the shear layer emission is boosted while the jet spine is

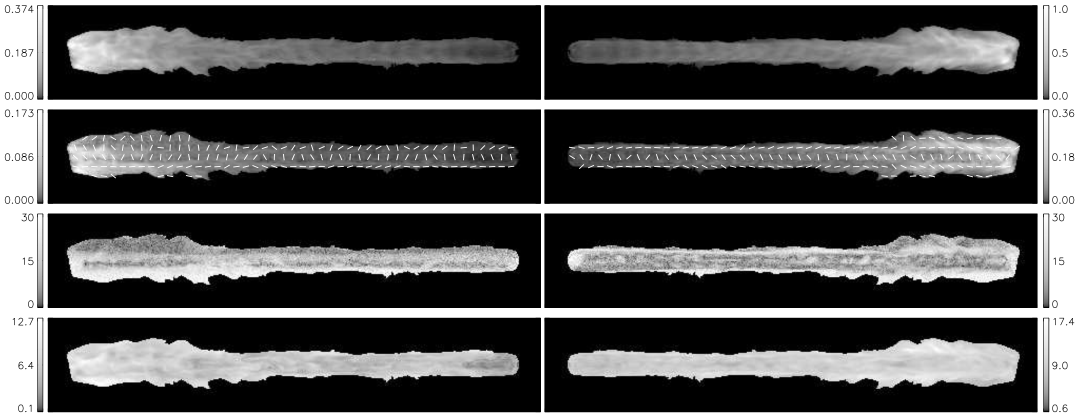

Fig. 3.20.— From top to bottom, panels showing the total intensity, polarized intensity, degree of polarization, and mean Doppler factor for a jet viewed at an angle of 50° (right panels) and its counterjet (left panels). Averages along the line of sight for each pixel, using the emission coefficient as a weight, have been used to plot the Doppler factor. The total and polarized intensities (in units normalized to the maximum in the main jet total intensity) are plotted in a square root scale. The bars in the polarized intensity panels show the direction of the magnetic field.

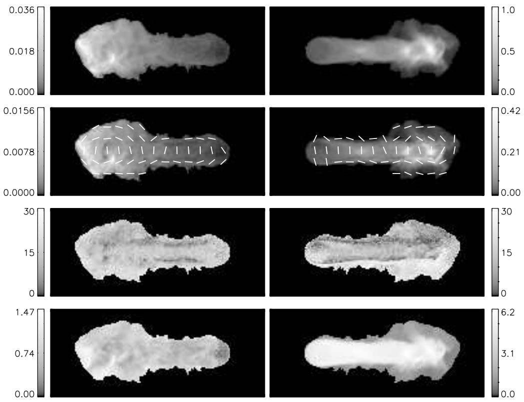

Fig. 3.21.— Same as Fig. 3.20, but for a viewing angle of 10°.

dimmed, as shown in the Doppler factor panel in Fig. 3.20. Cross section profiles of the jet emission at different viewing angles are plotted in Fig. 3.22, where the limb brightening effect can be more easily observed. For smaller viewing angles, as corresponding to Fig. 3.21, the jet spine emission is boosted, while the shear layer emission appears dimmed. Details of the jet spine can then be observed, as for instance two recollimation shocks, situated at $26R_b$ and $50R_b$. The jet emission then becomes spine brightened, instead of limb brightened, as observed in Figs. 3.21 and 3.22.

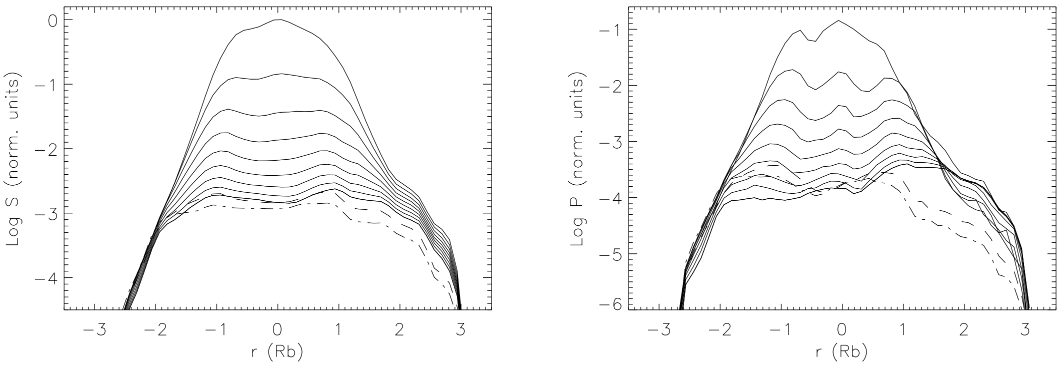

Fig. 3.22.— Logarithm of the integrated total (*left*) and polarized (*right*) intensity across the jet for different viewing angles. Lines are plotted in intervals of 10° from an angle of 10° (top line in both plots), to 90° (showing a progressive decrease in emission). Dashed lines (dot dashed) correspond to an observing angle of -100° (-140°). Positive beam radii correspond to the top in the images of Figs. 3.20 and 3.21. Units are normalized to the maximum in total intensity.

The same arguments apply to the polarized flux and, therefore, we obtain the same limb brightening for large viewing angles, and spine brighting for smaller values. As a result of the helical field in the shear layer, the apparent orientation of the magnetic field at the jet edges is parallel to the jet axis. For the jet spine, the toroidal and radial components of the magnetic field yield a net polarization perpendicular to the jet axis. As observed in Figs. 3.20 and 3.22, for relatively large angles the aligned component of the helical magnetic field in the shear layer projects into the jet spine partially canceling its field, yielding a smaller net polarization, stressing the limb brightening. Rails of low polarization can be observed where the apparent magnetic field rotates between being parallel (in the shear layer) to perpendicular to the jet axis, as observed in 3C353 (Swain, Bridle, Baum 1998).

Some of the kinematical and physical properties of the jet can be deduced by analyzing the jet/counterjet emission ratio, as plotted in Fig. 3.23 corresponding to

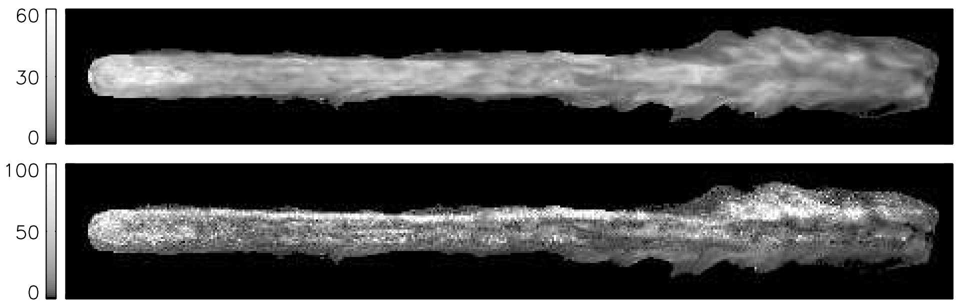

Fig. 3.23.— Total (*top*) and polarized (*bottom*) intensity jet/counterjet ratios for the jet models of Fig. 3.20. Polarized ratio is saturated at 100.

the jet model of Fig. 3.20. Jet deceleration is apparent as a progressively decrease in the total flux ratio along the jet axis. The velocity stratification across the jet is also visible as a decrease of the flux ratio close to the jet edges, that is, in the shear layer. This is visible in the inner jet region, while further down the jet, when the jet spine and shear layer velocities are more similar (due to the jet deceleration), the flux ratio is more uniformly distributed across the jet. The slower velocity in the shear layer and its high emission coefficient result in a smaller global flux ratio between the jet and counterjet than for the case of a "naked" high velocity jet spine (see also Komissarov 1990). This is because the shear layer emission is less affected by the viewing angle, that is, the Doppler factor.

3.3.2.2. Jet cross section emission asymmetry

Because of the helical magnetic field structure in the shear layer, an asymmetry in the emission appears across the jet. This asymmetry is more pronounced in the polarized emission, and is a function of the viewing angle, as shown in Fig. 3.22. In order to understand this effect we need to study the variation across the jet of the angle between the magnetic field and line of sight *in the fluid frame*, ϑ. The synchrotron radiation coefficients are a function of the sinus of this angle (see Eq. D3), and asymmetries in the distribution of ϑ will be translated into the emission maps. In order to compute ϑ we need to Lorentz transform the line of sight from

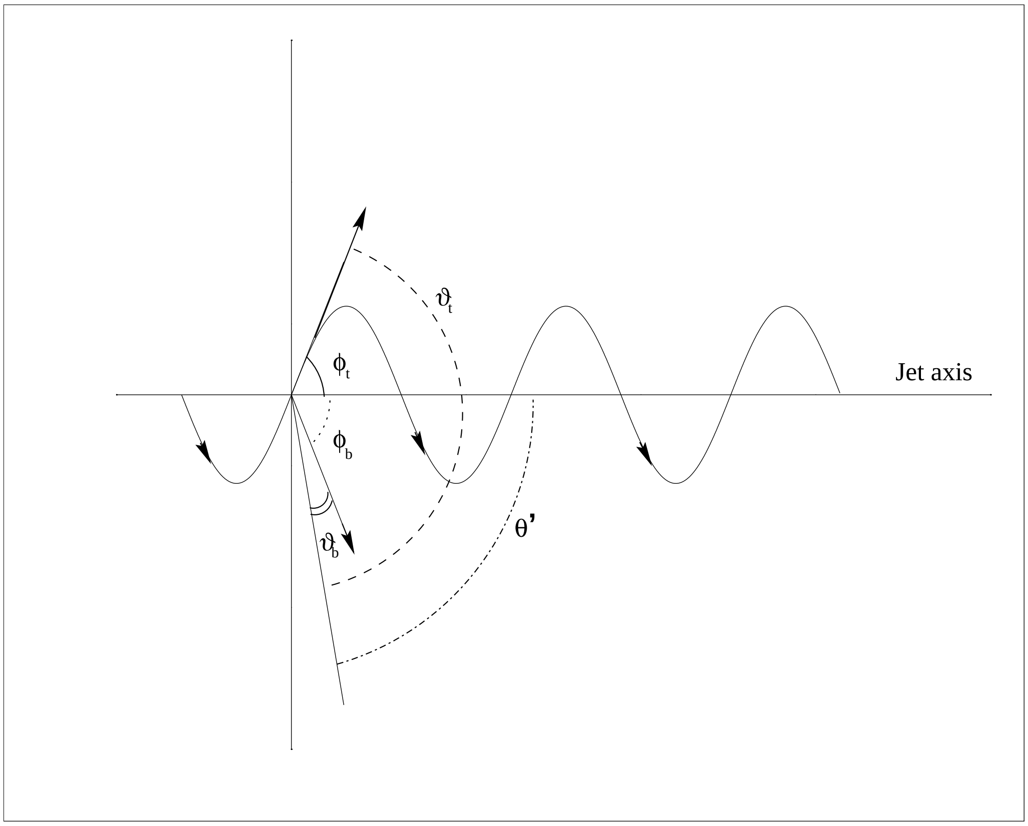

Fig. 3.24.— Relationship between the pitch angles (ϕ_t and ϕ_b) and the angles between the magnetic field and line of sight in the fluid frame (ϑ_t and ϑ_b). θ' is the angle to the line of sight in the fluid frame. The solid line represents the projection over the plane of the sky of the helicoidal magnetic field.

the observer's to the fluid's frame (see e.g., Rybicki & Lightman 1979)

$$\sin\theta' = \frac{\sin\theta}{W(1-\beta\cos\theta)} \quad , \quad \cos\theta' = \frac{\cos\theta - \beta}{(1-\beta\cos\theta)}$$

where θ' is the viewing angle in the fluid frame. Consider an helical magnetic field with a pitch angle ϕ, measured with respect to the jet axis (see Fig. 3.24). The angles ϑ^t and ϑ^b (where upper-script t and b refer to the top and bottom of the jet, respectively) differ by 2ϕ. Therefore, as long as ϕ is not zero or $\pi/2$, that is, the field is not pure aligned or toroidal, the $\sin\vartheta^{t,b}$ in the synchrotron radiation coefficients will introduce an asymmetry in the jet emission. This asymmetry will reach a maximum value for an helical magnetic field with $\phi = \pi/4$, as the one considered here. However, indistinctly of the helix pitch angle, the predominance between $\sin\vartheta^t$ and $\sin\vartheta^b$ will reverse at $\theta' = \pi/2$, which corresponds to a viewing angle in the observer's frame of $\cos\theta_r = \beta$. For an helical field oriented clockwise as seen in the direction of flow motion (i.e., the aligned component of the field is parallel to the jet flow), for $\theta' < \pi/2$ the bottom of the jet will show larger emission, while for $\theta' > \pi/2$ the top of the jet will be brighter (the opposite is true for an helical field oriented counter-clockwise, that is, with $\phi > \pi/2$). The maximum asymmetry will be obtained for $\theta' = \phi$ and $\theta' = \pi - \phi$, and the fastest transition (with changing θ') between top/bottom emission predominance will be obtained for ϕ close to $\pi/2$, that is, when little aligned field is present.

In the model we are considering, the shear layer has a mean $W \sim 1.7$, and therefore $\theta_r \sim 36°$. Smaller angles will show bottom jet dominance in emission, while for larger values the top of the jet will appear brighter. This is more clearly visible in Fig. 3.22. Note also that for the counter jet the helical field rotates opposite to the main jet, and therefore the jet asymmetry emission reverses. This is particularly well observed in the plot of the polarized emission ratio between the jet and counterjet of Fig. 3.23.

Although the $\sin\vartheta$ factor affects to both, total and polarized emission, the asymmetry is more clearly present in the polarized flux (see Figs. 3.20, 3.22, and 3.23). This is due to: i) The presence of randomly oriented magnetic field component, which renders the magnetic field distribution more homogeneous in the jet and diminish the asymmetry. ii) Smaller values of ϑ, indistinctly if present at the top or the bottom of the jet, always represent a larger variation of the magnetic field orientation along the line of sight, which in practice represents a larger degree of randomness in the magnetic field along the integration columns, decreasing the net polarization.

It is interesting to note that for $\theta \sim \theta_r$, small changes in jet velocity or viewing angle will produce a flip in the top/bottom jet emission dominance. For fast jets, θ_r will be accordingly small, and we will be biased towards observing jets with top emission predominance (as long as the helical field rotates clockwise as seen in the direction of flow motion).

An interpretation of the polarization observations of the blazar 1055+018 by

ARW99) can be obtained in terms of the model presented here. For that, we need to assume that 1055+018 is oriented close to θ_r, and contains a shear layer with helical field. If the helical field is oriented clockwise, the polarized emission observed at the top of the jet in inner regions would require that initially $\theta > \theta_r$, or $\theta' > \pi/2$. To obtain the opposite situation further down the jet, θ' has to become smaller than $\pi/2$, and for that either θ decreases, or θ_r increases, which requires that β decreases. Another third possibility, but that we find less plausible, is that the helical field in the shear layer changes orientation, that is, the pitch angles becomes larger that $\pi/2$. Therefore we can successfully explain the flip in the top/bottom orientation of the polarization asymmetry in 1055+018 if the jet bends towards the observer, or if decelerates. ARW99, and references therein) report the existence of bends in the jet of 1055+018. This support our hypothesis, but at the location of the flip in the polarization emission asymmetry, the jet spine emission decreases abruptly, contrary to what it would be expected in the case of a bend towards the observer, which should increase the jet spine emission by differential Doppler boosting. ARW99 obtained significantly larger apparent velocities for components closer to the core, suggesting a deceleration along the jet. Therefore, this points to our hypothesis of jet deceleration as the most plausible for the sudden change in polarization predominance between the top and bottom of the jet in 1055+018, since a jet deceleration will decrease the Doppler boosting, and hence the jet spine emission as observed. A relatively small aligned field (helical pitch angle close to $\pi/2$) will help to obtain such a fast flip in the polarization asymmetry with a relatively small jet deceleration.

Future observations of jet stratification in FRI and FRII sources should provide the necessary information to obtain a more detailed comparison with numerical simulations, helping to understand the nature of the shear layer, which as we have shown, plays an important rôle in the emission of relativistic jets.

3.3.3. Discussion and conclusions

We have analyzed the morpho-dynamical properties of a set of 3D relativistic jets. From our simulations, we can conclude that the coherent fast backflows found in axisymmetric models are not present in 3D models. We have investigated the beam's response to non-axisymmetric perturbations to check its stability. During the period of time studied by us ($t\lesssim 150 R_b/c$), the beam does not display the strong perturbations (particularly the filamentation of the beam) found by other authors in classical jets (Norman 1996, Hardee 1996) and it propagates according to the 1D estimate. Small 3D effects in the relativistic beam give rise to a lumpy distribution of apparent speeds like that observed in M87 (Biretta, Zhou & Owen 1995).

Our study must be extended to a wider range of models and perturbations. In particular, stronger perturbations should be considered to reach the nonlinear regime and to identify the acoustic and mixing phases (Bodo 1998) leading to the jet disruption. Further investigation also requires the dependence of the shear layer properties on the perturbation parameters. Finally, appropriate perturbations can be studied that mimic the wiggles observed in specific sources both at pc (0836+710, Lobanov *et al.* 1998; 0735+178, Gómez *et al.* 1999) and kpc scales (M87; Biretta, Zhou & Owen 1995).

We have also analyzed the properties of the boundary layer present in our models, both considering purely its hydrodynamics and their emission properties. From a dynamical point of view, the shear layer has appeared naturally in our model without being induced initially. The hydrodynamical jet structure agrees with the two-component models of Komissarov (1990) and Laing (1996), although the relatively high energy in the layer is a new element that leads to important observational consequences. Concerning the emission properties, these are closely linked to the *ad hoc* magnetic field configuration, and such fact has allowed us to interpret the ARW99 observations of 1055+018.

Other configurations of the magnetic field should be proven to reproduce particular features of current observations and, of course, the influence of the hydrodynamical model used to calculate the emission has to be investigated. A natural extension of the work would be to study the emission properties of the highly perturbed models in order to see if the characteristics of the shear layer emission persist when the central spine is highly distorted. These results will be reported elsewhere (Aloy *et al.* 2000).